Numerical Study of RKKY/Kondo Transition on Edges of Quantum Spin Hall Samples

Michael Franz Lichtenegger

München 2019

Numerische Analyse von RKKY/Kondo-Übergang auf Kanten von Quanten-Spin-Hall-Proben

Michael Franz Lichtenegger

München 2019

Numerical Study of RKKY/Kondo Transition on Edges of Quantum Spin Hall Samples

Michael Franz Lichtenegger

Masterarbeit
an der Fakultät für Physik
der Ludwig–Maximilians–Universität
München

vorgelegt von
Michael Franz Lichtenegger
aus Regensburg

München, den 18.02.2019

Erstgutachter: Prof. Dr. Jan von Delft
Zweitgutachter: Dr. Oleg Yevtushenko

Acknowledgement

In preparation of my project, I engaged the service and guidance of some respected persons who deserve my deepest gratitude. As the completion of this assignment gave me much pleasure, I would like to show my gratitude to my supervisor Oleg Yevtushenko for giving me good guidelines for my project within numerous consultations.
I would also like to express my gratitude to all those who have directly and indirectly guided me in writing my thesis.
Seung-Sup Lee, who introduced me into the field of NRG and offered me his codes to use throughout the project. He always had an open ear for my problems.
Andreas Weichselbaum for fruitful discussions and helpful advise on how to connect physics and numerical considerations.
Jan von Delft for the hospitality at his chair providing me a office.
Dennis Schimmel for helpful discussions during the beginning of the project.
Elias Walter in his special job as our IT supervisor who helped me with several upcoming cluster problems.
My roommates Dima Pimenov, Sebastian Huber, Johannes Feldmeier and Julian Thöniß who never hesitated to get engaged in subject-specific discussions with me. The pleasant atmosphere in our office made the work on my thesis a lot more enjoyable.
And, last but not least, all the others members of the von Delft chair for the productive atmosphere.

Abstract

Subject of this study are two Kondo impurities coupled to helical edge modes of 2D time-reversal invariant topological insulator. The latter is described by using a Kane Mele lattice model. Helicity is defined as a lock in relation between spin and propagation direction. an edge with a specific helicity supports only modes which share the same helicity.
The physics of such a system are determined by a competition of two seminal phenomena: The Kondo effect and the Ruderman-Kittel-Kasuya-Yosida (RKKY) indirect exchange interaction.
The Kondo effect leads to a screening of the impurity spins by itinerant conduction electrons for each impurity separately whereas the RKKY indirect exchange interaction correlates them. The Kondo/RKKY competition has intensively been studied in the literature starting with the seminal paper by Doniach [1]. The Kondo phase is normally suppressed in 1D usual systems, thus the RKKY phase dominates in a huge range of Kondo couplings and interimpurity distances.
However, the Kondo/RKKY competition in a 1D helical Luttinger liquid (HLL) is highly nontrivial [2]. Namely, the Kondo effect can be enhanced significantly by magnetic anisotropy or Coulomb interaction. The latter is typically strong in realistic samples. One can come across the case where the Kondo effect overwhelms the RKKY interaction even at small distances. This behavior can be explained with Doniach's criterion. The two characteristic energy scales of the RKKY indirect exchange interaction (the RKKY energy) and the Kondo effect (the Kondo temperature) can be used to compare the two effects. If the RKKY energy is greater than the Kondo temperature, the RKKY phase will win. However, the Kondo temperature can be significantly increased in HLL, thus the Kondo effect is possibly superior to the RKKY phase.

The current project is devoted to a numerical study of a two impurity Kondo model coupled to helical edge modes of a quantum spin Hall system via NRG calculations. Numerical treatment is needed as a complimentary tool to the existing analytical theory [2] to investigate a real lattice model which can not be included in the analytical considerations. Furthermore, analytics addressed only limiting cases far from the RKKY/Kondo transition (e.g. decoupling limit for the Kondo description). A detailed theory of RKKY/Kondo transition do not exist.
Numerics include evaluating energy flow diagrams (outcome of NRG calculations), calculating interimpurity spectral functions and expectation values of interimpurity operators $\langle S_1^z S_2^z \rangle$.
These methods has allowed us to study the RKKY/Kondo transition for this particular model because the expectation value of the interimpurity operator differs in the RKKY phase compared to the Kondo phase.
The main result of the current project is the numerical confirmation of the analytically obtained predictions of the RKKY/Kondo competition in a helical 1D system [2]. In that paper, a RKKY/Kondo transition is predicted for an effective Luttinger parameter of $\tilde{K}_a = 1/2$ whereas the numerical calculation during this project obtains a critical effective Luttinger parameter of $\tilde{K}_n \approx 3/4$.
The difference can be explained with the use of different models in analytical and numerical studies as well as with the phenomenological nature of the Doniach criterion which can only yield an approximate value of the critical Luttinger parameter.

Contents

List of Figures

Chapter 1

Introduction

In the last decades the finding of new kinds of phases in condensed matter physics was a cornerstone in the research for sophisticated materials [3]. These substances can be used for new applications in spintronics [4]. Compared to phases that have been well known before these ones are characterized by their topology. The topological class is characterized by a topological invariant which is specific for a given system and for given symmetries. As long as the specific value of this invariant does not change, the same physics can be expected. Because of the similarities to the mathematical definition, where some elements of the same topology can be transformed (with some allowed manipulations) but stay in the same topology, the name topological phase is suitable in physics, too. If, for instance, the genius is considered as the topological invariant, 3D objects with the same genus belong to the same topology class. Thus, a cup and a torus will be in the same topology, they have 1 hole, wheres a pretzel will not be in the same topology. In physics, a change of the topology invariant value can be caused by a gap closing of a dispersion relation which changes the phase from a topological trivial to a non trivial one [3] or vice versa.
One of these discovered topological classes was rewarded by a Nobel prize in physics to Haldane, Thouless and Kosterlitz in 2016. Von Klitzing et al. experimentally discovered the integer quantum Hall effect (IQHE) [5] awarded with the Nobel prize 1985, which is a nontrivial topological phase and supports chiral modes on the spatial boundaries.
Haldane suggested a possible lattice model realization of the IQHE without applying an external magnetic field [6].
A further step was taken by Kane and Mele who suggested a lattice model which realizes the quantum spin Hall effect (QSHE), also known as topological insulator (TI), in graphen [7]. The topological invariant of a quantum spin Hall system is isomorph to the $\mathbb{Z}_2$ group. The TI has gapped bulk states, but supports helical edge states on its boundaries. They are gapless states which traverse the same edge in opposite directions for different spins. Thus, their helicities $= spin \times cirality$ are equal [8, 9, 10, 11] and are defined as ± 1.
Helicity is defined as a lock in relation between group velocity and spin. On the other edge, there exist modes with opposite helicity ∓ 1. The TI is time reversal symmetric (TRS) [9] in contrast to Haldane's model where TRS is broken.
The trivial topological phase would be a complete gaped spectrum.
Due to their finite gap, the bulk states are irrelevant for low energy physics [8]. Interesting physics happens on the boundary of a 2d TI, where the helical edge states are located. The fixed helicity for the edge states protect electrons from backscattering off a nonmagnetic scatterer. This is due to the fact that backscattering can only appear if it is accompanied by a spin flip of the electron. This is only possible, if a magnetic impurity is involved as a scatterer.
The system studied in this thesis is a non-interacting Kane Mele system with magnetic impurities attached to the honeycomb structure. The Kane Mele system will be in the non trivial topological phase, if proper parameters are chosen.

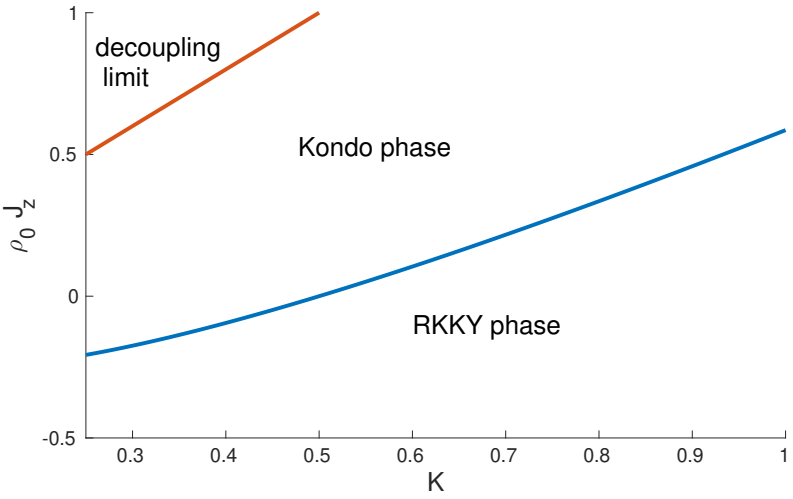

Figure 1.1: Phase diagram of the two impurity Kondo model (see Fig.1 in [2]). The system parameters are the Luttinger parameter K and the dimensionless anisotropic Kondo coupling $\rho_0 J_z$. The Kondo coupling $\rho_0 J_\perp$ stays fixed.

The goal of this work is a numerical confirmation of analytic obtained results contained in [2]. In this paper, analytical calculations are done for a system consisting of a helical Luttinger liquid. Two Kondo impurities (i.e. spin-spin interaction of bath electrons and impurity) are coupled to the helical Luttinger liquid.
The paper explained in the abstract of V. Judson and O. Yevtushenko suggests a competition between a regime where the leading interaction results from the RKKY interaction and a regime where the system is Kondo screened, hence it is in the Kondo phase [2] (i.e. magnetic impurities are screened by itinerant electron spins). The argumentation of [2] follows a well proofed statement of Doniach which states a criterion to distinguish the RKKY from the Kondo regime [1].
The different phases are depicted in the phase diagram Fig. 1.1.
Backscattering in a topological insulator is only possible if magnetic impurities such as Kondo impurites are involved. Forward scattering can be included into the description by introducing an effective interaction. Thus, the system is fully described by an effective interaction parameter $\tilde{K}$ (depending on the forward scattering Kondo coupling constant J_z) and the backscattering Kondo coupling $J_\perp$. This absorption of forward scattering into an effective Luttinger parameter is not possible for non helical Luttinger liquids, hence the Kondo effect can not be enhanced by introducing anisotropy which will be used during this thesis.
The model is tackled by the numerical renormalization group (NRG) method. Equipped with this method, one can calculate different physical observables. Subject of the present study is the numerical analysis of correlation functions (more accurate spectral functions which are the imaginary part of the correlation functions), like the correlation function in [2], numerically.
This correlators are the interimpurity retarded Greens function $\langle S_1^z S_2^z \rangle$ and the local on $\langle S_1^z S_1^z \rangle$, where the lower index marks which impurity spin operator is considered (i.e. first or second impurity).

The suggested crossover between a Kondo regime and a Ruderman-Kittel-Kasuya-Yoshida (RKKY) regime should be detected.
This can be realized by changing the system parameters from isotropic to anisotropic Kondo coupling and driving the interaction parameter J_z (see Fig. 1.1) to strong anisotropy [2].
Another way to observe the crossover contains the change of the interimpurity distance. The Kondo temperature is independent of the interimpurity distance [1]. But the RKKY energy decreases for increasing separation of the impurities. Thus, the RKKY energy can be lowered in this

way and one can try to suppress it even below the Kondo temperature which drives the system to the Kondo regime.

1.1 Goal of the thesis

This project is devoted to a numerical study of a two impurity Kondo model coupled to helical edge modes of a quantum spin Hall system using NRG calculations.
A proper lattice model which supports helical edge modes has to be chosen. The edge modes have to be localized very close to the edges and their helicity should be guaranteed.
In our case, we chose the Kane Mele lattice model because it provides helical edge modes according to our numerical investigation.
The main goal of the project is a numerical confirmation of the analytically obtained predictions of the RKKY/Kondo competition in a helical 1D system [2] by using the model type mentioned above.
The intermediate goals for achieving the aforementioned are calculating the Kondo temperature for a single Kondo impurity model, estimating the RKKY energy for a two Kondo impurity model and comparing them afterwards. Those two energy scales are the characteristic energy scales for each effect concerned. The reasoning for those goals is a criterion presented by Doniach [1] which can be used to make a statement about the dominant effect by comparing those characteristic energy scales. If the Kondo temperature is greater than the RKKY energy, the system is in the Kondo regime. For the opposite case, which is the usual one, physics are dominated by the RKKY indirect exchange interaction.
The Kondo effect can be highly enhanced in a 1D helical system if it is a strong interacting system. This interaction can be mimicked by applying strong anisotropic Kondo coupling in helical Luttinger liquids.
A critical effective Kondo coupling can be determined by driving the system into the Kondo dominant regime starting in the RKKY regime. This is done by means of increasing anisotropy J_z which is the forward scattering Kondo coupling.

Chapter 2

Introduction to the physics of topology and interacting systems

The following chapter presents the main ingredients and methods used during the project. It is supplemented by the Appendices where lengthy calculations are given which are excluded form the main text.
The outline is as follows: The thesis starts in Sect. 2.1 with topological non trivial systems and their realization in lattice models.
An introduction in 1d physics (Sect. 2.2) gives us a machinery to work with sophisticated methods to handle interacting systems with minimal approximations. This is an outstanding feature of 1d physics.
The edge modes of a topological insulator can be seen as a quasi 1d system, because the bulk modes are gapped.
The RKKY interaction is an interimpurity exchange interaction which is mediated by conduction electrons. The RKKY interaction and the Kondo effect (Sect. 2.3.3) are discussed in Sect. 2.3.2 and in Sect. 2.3.3 respectively.

Sect. 2.3.4 compares the RKKY interaction and the Kondo effect. They compete with each other. If the considered system is a helical one, the above mentioned competition changes qualitatively which is the topic of Sect. 2.3.5.
Finally (Sect. 2.4), the numerical renormalization group (NRG) method suggested by Wilson is introduced in Sect. 2.4. Results obtained with the help of this method are presented in Sect. 3.1.4 to solve the impurity problem (i.e. realistic lattice 2d model, 2 impurity Kondo model with anisotropy).

2.1 Topology matters

Physics of topological phases reflects global properties of quantum states in materials [11]. These global properties are symmetries which leaves the system Hamiltonian invariant under such symmetry transformation and the spatial dimension of the system. The space dimension constitutes the supported edge modes. A TI in two spatial dimension host helical edge states on its boundaries, where has a time reversal quasi one dimensional system supports edge modes at its boundaries which are points know.

To characterize these topological non trivial phases one can define a topological invariant. The quantum Hall effect can be described with the normal Chern number which is a $\mathbb{Z}$ number [8]. The spin Chern number characterizes the quantum spin Hall effect, it is out of the set $\mathbb{Z}/\mathbb{Z}_2$ [9]. Both are, in principle, measurable observables, that can be detected by state of the art experiments [5] [12].

If the magnitude of the topological invariant changes, e.g. between a trivial and a non trivial phase of a topological insulator, interesting physics can be detected. Zero energy edge modes are located at the interface between materials which have different topological invariant values. This appearance can be explained by the bulk boundary correspondence [13].
This section is devoted to give a short introduction to the huge field of symmetries in physics and their implications in terms of topology. The quantum spin Hall system is of mayor interest, because it hosts zero energy helical edge states on its spatial boundaries which serves as quasi 1d helical system latter on [7].

2.1.1 Symmetries

If a given system has a symmetry, its Hamiltonian commutes with the symmetry operator A which reflects the symmetry under consideration

$$[H(r), A] = 0. \tag{2.1}$$

The bracket is the commutator.
A non-trivial topological quantum phase is characterized by the spatial dimensionality of the system as well as special symmetries and their corresponding topological invariants [14].

In the following the time reversal symmetry (TRS) is considered. This symmetry can be represented by an anti-unitary operator [15] acting on the Hilbert space of the underlying system Hamiltonian.
This anti-unitary operator can be split into two operators. One of these operators is a unitary operator and the other one is complex conjugation, i.e. $\hat{T} = \hat{K}\hat{U}$ where $\hat{T}$ is the time reversal operator, $\hat{K}$ is complex conjugation and $\hat{U}$ is a unitary operator. These operators all act on the same Hilbert space.

The physical meaning of time reversal symmetry is that there is no difference for the system to evolve from a point of time in the past to one in the future or vice versa. Thus no measurable quantity (observable) depends on the time axis direction.
If one considers an electron flying in free space with a fixed velocity, the system will be TRS. Whereas the system will not be TRS if a magnetic field perpendicular to the electron's flying direction is applied.

The time reversal operator for a system consisting of spinful fermions ($S = 1/2$) [10] is

$$\Theta = -i\sigma_y K. \tag{2.2}$$

In this case, K is complex conjugation and σ_y is a Pauli matrix in spin space. Note, that the above mentioned unitary operator is $\hat{U} = -i\sigma_y$ in this context.
A time reversal symmetric Hamiltonian fulfills

$$H(-\vec{k}) = \Theta H(\vec{k})\Theta^{-1}. \tag{2.3}$$

For example, the topological insulator (TI) is a time reversal symmetric system see below ,e.g. Kane Mele lattice model, whereas TRS is broken for systems supporting the integer quantum Hall effect, see below e.g. Haldane's lattice model).

2.1.2 Graphene

The following section introduces graphene, which its honeycomb lattice structure serve as a basis for lattice model realizations of topological non trivial states (e.g. Kane Mele Model). Its Hamiltonian is

$$H_{Graphen} = t \sum_{<ij>} c_i^\dagger c_j + \sum_i \mu_{A/B} c_i^\dagger c_i, \tag{2.4}$$

where the sum runs over its nearest neighbor's sites and t is the hopping term between those sites. Nearest neighbor hopping does not take place within the same sublattice depicted in Fig. 2.1 (hopping from a red to a blue site). The second term introduces a sublattice potential which is dependent on the lattice site species $\pm\mu$.
The spatial lattice structure is of the form of a honeycomb, thus consists of hexagons. In Fig. 2.1 the unit cell for a confined graphene lattice is depicted (unit cells are separated by vertical solid lines), where there are 6 sites in the unit cell for this specific confinement. Open boundary conditions (OBC) are applied along the vertical direction and periodic boundary conditions (PBC) are applied along the horizontal direction. The distance between two neighboring unit cells is $a_1 = \sqrt{3}a$, where a is the graphene lattice constant.
The Hamiltonian for graphene Eq. (2.4) is time reversal symmetric.

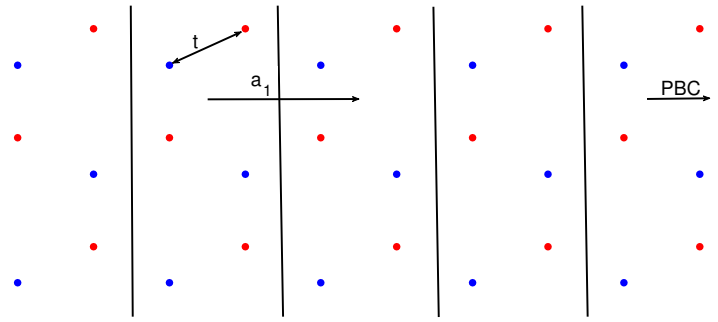

Figure 2.1: This figure shows the lattice structure of grahene with 2 horizontal zigzag boundaries. The vertical lines mark the unit cell. a_1 is the distance between 2 unit cells and t is the nearest neighbor hopping term. The red/blue points mark a sublattice.

The Fourier transform of the single particle creation operator is

$$c^\dagger_{xy} = \frac{1}{N_x}\sum_{k_x} e^{ik_x x} c^\dagger_{k_x y}, \tag{2.5}$$

and the corresponding Fourier transformed Hamiltonian of graphene [10]

$$H(k_x) = -t\sum_j \left(c^\dagger_{2jk_x} c_{2j+1k_x} + h.c.\right) - t\sum_j c^\dagger_{2jk_x} c_{2j-1k_x} \left((e^{ik_x a_1} + e^{-ik_x a_1}) + h.c.\right). \tag{2.6}$$

The j sum runs through all sites within the unit cell of graphene. The unit cells are separated from eachother with the vertical solid lines in Fig. 2.1.
There are flat bands (i.e. 2 for two edges, neglecting spin) between the two Dirac points [16] $K = 2\pi/3a_1$ and $K' = 4\pi/3a_1$ at the Fermi level depicted in Fig. 2.2(a). By turning on a sublattice potential a trivial gap opens at the two Dirac points which is shown in Fig. 2.2(b) where the edge modes do not traverse over the Fermi level (0 energy level). I.e. a topological trivial gap is introduced by a sublattice potential [10][11]. There are as many bands as sites in the unit cell (in the figure there are 80 sites within the unit cell). By increasing the amount of sites within the unit cell, the bulk bands get denser in the bulk.
Based on the graphene lattice structure, Haldane suggested a realization of the Integer quantum Hall effect which is the topic of the following section.

2.1.3 Integer quantum Hall effect (IQHE)

The integer quantum Hall effect is the first upcoming example in this thesis for a topological state of quantum matter [17].
The integer quantum Hall effect arises when electrons are confined to 2d and a magnetic field

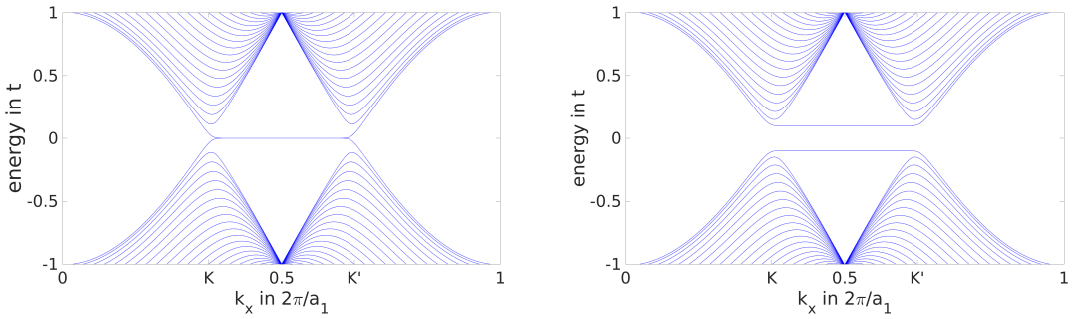

(a) Graphene without a gap

(b) Graphene with a gap

Figure 2.2: The band structure of graphene along the quasi impulse k_x. The two Dirac points K and K' are connected via a flat band which consists of the edge modes (a). In (b) a trivial band gap opens due to a sublattice potential of $\mu = 0.05$.

is applied [5]. This state is not a usual insulating nor a metallic phase. The electron energy spectrum splits into so called Landau levels due to the perpendicular applied magnetic field [18]. The spectrum is

$$\epsilon_n = \omega_c \hbar (n + 1/2), \tag{2.7}$$

with $\omega_c = qBe/mc$ being the cyclotron frequency and n being an integer. For the case that N Landau levels are filled and the others are empty, there is gap between the valence and conduction band like in an ordinary insulator. But if one applies an electric field, the cyclotron orbits drift (skipping orbitals) which leads to a Hall current. This Hall current is quantized and the corresponding conductivity is

$$\sigma_{xy} = Ne^2/h. \tag{2.8}$$

This astonishing result was confirmed by von Klitzing et al. experimentally [5].
The skipping orbitals are located at the edges of the 2d system. The conduction carrier mode is also located at the edge and is chiral in the following sense. The direction of the supported mode is determined by the given edge and the direction of the perpendicularly applied magnetic field. The second edge supports the counter propagating mode, with a respectively opposite group velocity (i.e. opposite sign, direction) as the aforementioned first chiral mode.
If the magnetic field is applied in opposite direction, the chiral modes will change there direction as well. Thus, each edge can be assigned by a chiral quantum number characterizing the edge state. This chiral quantum number serves as a topological invariant which is stable within the above given topology definition.

Haldane suggested a 2d lattice model, which is in the quantum Hall phase without an external applied magnetic field [6].
The net magnetic flux in Haldane's unit cell is 0, but at each lattice site there is a non zero magnetic flux which breaks time reversal symmetry. This lattice model consists of a honeycomb structure (like Fig. 2.1), where nearest neighbor sites are of different type (A/B). An inversion symmetry breaking on site energy term μ can also be considered (see Sect. 2.1.2).
Haldane included one more hopping term into the model which is a next nearest neighbor contribution t_2 . This hopping is within the same sublattice (i.e. A/A or B/B) and can be assigned with a phase (i.e. $t_2 \in \mathbb{C}$). This phase factor generally breaks the time inversion symmetry (for special phase factor values the time inversion symmetry will remain, e.g. $t_2 \in \mathbb{R}$). Haldane's lattice model Hamiltonian is

$$H_H = t_1 \sum_{<ij>} c_i^\dagger c_j + t_2 \sum_{\ll ij \gg} c_i^\dagger c_j + \sum_i \mu_{A/B} c_i^\dagger c_i, \tag{2.9}$$

with $\mu_{A/B} = \pm\epsilon$ being different for a specific sublattice (A or B) and the two hopping terms, nearest neighbor t_1 and next nearest neighbor t_2 denoted by $< ij >$ and $\ll ij \gg$, respectively.

As mentioned before, the system described by Eq. (2.9) is a lattice model in 2d. The quasi impulse is a good quantum number. Thus, one can Fourier transform Haldane's real space Hamiltonian Eq. (2.9) to end up with [10]

$$H_H(\vec{k}) = c^\dagger(\vec{k})[t_1 \sum_i^3 (\cos(\vec{k}\vec{a}_i)\sigma^x + \sin(\vec{k}\vec{a}_i)\sigma^y) + \\ + \sum_j^6 (t_2 \cos(\phi)\cos(\vec{k}\vec{b}_j)\sigma_0 + (M/6 - t_2 \sin(\phi)\sin(\vec{k}\vec{b}_j))\sigma^z)]c(\vec{k}). \tag{2.10}$$

Here, ϕ is the phase factor of the imaginary hopping t_2, $\vec{k}$ is the quasi momentum, $\vec{a_i}(\vec{b_j})$ the 3(6) displacement vectors, which connect a B(A) site to its 3 nearest neighbors A sites. The $\sigma^{(x,y,z)}$ are Pauli matrices and $\mathbb{I}$ is the identity in sublattice space, so the diagonal terms correspond to hopping within the same sublattice and the off-diagonal ones correspond to inter sublattice hopping (A/B or B/A). Thus, the sublattice space serves as a pseudo spin.

2.1.4 Quantum spin Hall effect (QSHE)

The quantum spin Hall effect (QSHE) has a charge excitation gap within the bulk, but has symmetry protected 1d gapless edge states which lie inside the bulk insulating gap [19].
The edge states counterpropagate along the same edge for opposite spin, thus they are called helical edge modes (propagation direction and spin are connected).
The helical edge modes appear as Kramers doublets.
The Kramers degeneracy theorem states that for a time reversal invariant spin-1/2 system (e.g. QSHE system), there are always two states which share the same energy.
TRS ensures the crossing of their energy levels at special points (Dirac points) in the Brillouin zone. Because of this level crossing, the spectrum of a QSH insulator cannot be adiabatically deformed into that of a topologically trivial insulator without helical edge states. Therefore, in this sense, the QSH insulator represents a new topologically distinct state of matter.
The topological properties of the QSH state can be characterized by the spin Chern number [20]. More generally, the topological properties of the QSH state are mathematically characterized by a $\mathbb{Z}_2$ topological invariant [9]. Physical systems with an even number of Kramers pairs of edge modes at a given boundary are topologically trivial, while those with an odd number are topologically nontrivial [8].

Kane and Mele suggested a realization of the QSHE in a real lattice model [7]. Based on the graphene lattice structure and the considerations of Haldane, they considered a next nearest neighbor hopping which is time reversal symmetric. Thus, the whole Kane Mele model is time reversal symmetric. A property which does not generally exist in the Haldane lattice model, it explicitly breaks time reversal symmetry (see Sect. 2.1.3).
The quadratic Kane Mele Hamiltonian is

$$H_{KM} = t \sum_{<ij>\sigma} c^\dagger_{i\sigma} c_{j\sigma} + it_{so} \sum_{\ll ij \gg \sigma\sigma'} \nu_{ij} c^\dagger_{i\sigma} S^z_{\sigma\sigma'} c_{j\sigma'} + \mu_{A/B} \sum_{i\sigma} c^\dagger_{i\sigma} c_{i\sigma}. \tag{2.11}$$

The sum of the first term in Eq. (2.11) runs over nearest neighbors and spins, whereas the second sum runs over next nearest neighbors and spins. The ν_{ij} characterizes the sign of the next nearest neighbor hopping, it takes the value of $+1$ for counter clockwise or -1 for clockwise hopping depicted in Fig. 2.3. It reflects the hermitian conjugation in the given notation $\ll ... \gg$. If it is missing, the Hamiltonian will not be hermitian.
The $S^z_{\sigma,\sigma'}$ is the z Pauli matrix which is diagonal and consists of the entries $+1/-1$ for the spin up/down component.
The last term is diagonal in real and spin space, and represents a sublattice potential. $\mu_{A/B}$ takes different values for sites of type A or type B (in Fig. 2.3 the red (A) and blue (B) sites constitute a sublattice for each site species).

The Hamiltonian defined in Eq. (2.11) is time reversal symmetric. The reason for this lies in the fact that Kane and Mele included a non trivial spin dependency in their system (i.e. the next nearest neighbor hopping in Eq. (2.11)). The time reversal operator Θ is defined in Eq. (2.2)).
The non trivial part of the Kane Mele Hamiltonian transforms under time reversal like

$$\begin{aligned} \Theta it_{so} S^z \Theta^{-1} &= (-i\sigma^y K)(it_{so} S^z)((i\sigma^y K)) \\ &= -it_{so} \sigma^y S^z \sigma^y KK = -it_{so}(-S^z) = it_{so} S^z. \end{aligned} \tag{2.12}$$

The other terms of the Kane Mele Hamiltonian are real and diagonal (proportional to the identity) in spin space, thus these terms transform trivially under time reversal.
This leads to

$$\Theta H_{KM} \Theta^{-1} = H_{KM}, \tag{2.13}$$

which shows that the Kane Mele Hamiltonian is time reversal invariant.

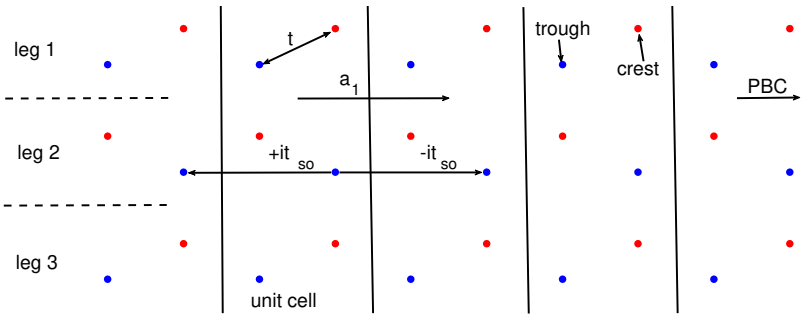

Figure 2.3: The confined Kane Mele lattice model with nearest neighbor hopping t and imaginray next nearest neighbor hopping t_{so} is depicted. The next nearest neighbor hopping is dependent on the hopping direction, it is negative for clockwise and positive for counter clockwise hopping. Legs are separated via the dotted lines. The unit cell is within two vertical solid lines and consists of $2 \times N$ sites (N being the amount of legs, 3 in this case) for the finite Kane Mele model. The crest sites are the outermost sites on the leg edge, the trough sites are the innermost sites on the leg edge.

In Fig. 2.3 the spatial lattice structure of the finite Kane Mele model is depicted. The hopping terms are denoted by arrows, where the clockwise/counter clockwise dependence of the next nearest neighbor hopping is illustrated. For the depicted lattice structure 3 legs are considers which leads to 6 sites in the unit cell. Thus, the edges of this system consist of leg 1 and leg 3. The reason for the use of the nomenclature crest and trough sites becomes clear in further sections. Crest sites denote the outermost sites of the boundary, trough sites denote the innermost sites of the edge leg.
If one considers an odd number of legs (like in Fig. 2.3), the crest sites on the two boundary legs are not on spatial equivalent positions in x direction, whereas by considering an even amount of legs, the crest sites sit on spatial equivalent positions in x direction.

The band structure of the Kane Mele model is depicted in Fig. 2.4(a) (the band structure is the same as in the original paper of Kane and Mele [9]). There are zigzag boundaries applied along the OBC direction. The system consists of 40 legs, i.e. 80 sites per unit cell (constitutes the amount of bands), the next nearest neighbor hopping is $t_{so} = 0.03t$ and the nearest neighbor hopping determines the energy scale in which every energy is expressed $t = 1$. No sublattice potential is turned on so far, and PBC are applied along the horizontal direction.
The dispersion relation is plotted for both spins (up and down) which are degenerated (they lay on top of each other).
The 2 previous (for graphene) Dirac points K and K' are gapped, but the edge modes survive at 0 energy. The reason for this is that the introduced 2^{nd} neighbor hopping opens a gap. The mass term responsible for the gap has a inversed sign at K compared to K'. The helical edge modes corresponding to the same mass term has to cross the Fermi surface. Thus, K and K' are connected non trivial (crossing of the Fermi level) via the helical edge modes.

The edge modes cross each other at $k_x = \pi/a_1$ which serves as a new Dirac point in the Kane Mele model. In the vicinity of this point a linear dispersion can be assumed.
If one introduces a mass term which has the same sign at K and K', the Dirac points will be connected topologically trivial, where the Fermi level will not be crossed (as for the graphene model Fig. 2.2).
The mass term Δ depends linearly on t_{so} via $|\Delta| = 6\sqrt{3}t_{so}$ (whole gap size) [10].

If a sublattice potential $\mu = 0.01$ is turned on (i.e. for A sites it is $+\mu$ and for B sites it is $-\mu$), the energy degeneracy of different spins is lifted which is illustrated in Fig. 2.4(b).
Here, the blue curve depicts the spin down and the red curve the spin up band. The points where the helical edge states cross the Fermi level is shifted to higher/lower quasi impulses for

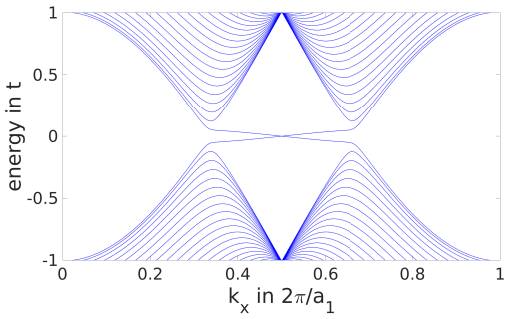

(a) Kane Mele dispersion relation for sublattice potential $\mu = 0.01t$. Spin up and spin down particles are degenerated

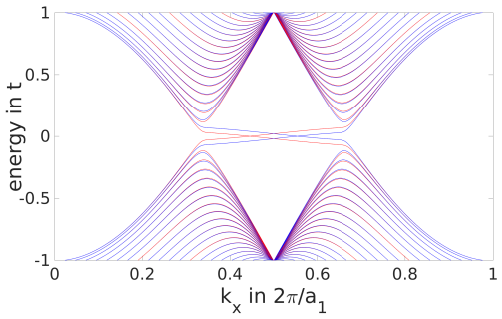

(b) Kane Mele dispersion relation for sublattice potential $\mu = 0.01t$. The spin degeneracy is removed

Figure 2.4: The band structure of the Kane Mele model with (a) and without (b) sublattice potential. The system consists of 40 legs and PBC are applied along the x direction. The next nearest neighbor hopping $t_{so} = 0.03t$ and the nearest neighbor hopping is t. The Dirac points of graphene K and K' are gapped now. Helical edge states traversing the Fermi level connect the K and K' non trivially. Panel (b) shows the dispersion relation of the Kane Mele model where a sublattice potential splits the degeneracy of spins. The red curve depicts spin up and the blue curve depicts spin down. The two crossing points at the Fermi level are shifted in opposite directions for different spins.

spin down/up. Up to this feature, the band structure is quite the same as without a sublattice potential. The bulk states are gapped and there are helical edge states.
If one further increases the sublattice potential $\mu/t_{so} > 3\sqrt{3}$, the system will be trivially gapped again [10].

The states which are located at exactly 0 energy (right at $k_x = \pi/a_1$ in Fig. 2.4(a)) are helical edge states. There are 4 helical edge states (2 Kramer doublets), their degeneracy is due to the 2 edges and 2 spin configurations for a spin-1/2 fermionic system.
Each edge hosts two states with different spin and different group velocities where their helicity is the same. If the bulk is big enough (i.e. there are many sites within the boundaries), the edge states of different edges are well separated from each other (i.e. their overlap is 0). The penetration of the edge state into the bulk decays exponential (see Fig. 3.1).
The above claimed statements about helical edge states at the edge of the Kane Mele model and the exponential decreasing penetration depth will be confirmed in Sect. 3.1.1.

2.2 1d physics

Physics in one spatial dimension are extraordinary compared to physics in higher dimensions. Fermi liquid theory is quite suitable for describing interacting electron systems in dimensions higher than 1 [21].
A Fermi liquid is a quasi free quasi particle theory if weak interactions are considered. The fundamental principle underlying the Fermi liquid theory is adiabatic continuity [22].This means a smooth evolution of a non-interaction ground state into an interaction one, if the interaction strength is increased. Thus, the excited state of the interaction system can be approximated by the non-interaction exited state. The excitations are particle hole excitations.

Essential for the validity of Fermi liquid theory is the stability of the quasi particle excitations near the Fermi surface. We deal with low energy physics nearby the Fermi surface.
This stability can be proven and shows that the lifetime of the quasi particles diverges close to the Fermi surface at $T \to 0$.
In $d = 1$ the Fermi liquid theory breaks down, the life time of electron hole excitation shrinks to zero if the excitation energy goes to zero (nearby the Fermi points). Thus the electron hole pair is not stable any more and decays in an uncontrolled fashion.
A natural question arises due to the above mentioned break down of Fermi liquid theory in 1d: Is there another suitable theory to describe interacting fermionic systems in 1d? Such a theory indeed exists. It is called Luttinger liquid theory where the excitations are collective modes (e.g. charge, spin). Bosonization is a technique which is applicable to Luttinger liquids and allows a transformation from fermionic degrees of freedom to bosonic ones [21]. It can be used to arrive at a Luttinger liquid Hamiltonian for long wavelengths (low energies).
By considering Luttinger liquids, the interaction of the electrons is included by the Luttinger parameter K and a renormalized velocity u.
If the desired system consists of spinful particles, adjustments of the above theory have to be done. However, the conceptual structure does not change [21].

The electron momentum density of states has a power-law non-analyticity at the Fermi point in 1d [23][21]. This is in sharp contrast to the usual discontinuity of the electron momentum density of states at the Fermi surface in Fermi liquids.
The reason for this different situation is that electron-electron interactions destroy this discontinuity in 1d [21].
The excitations in 1d consist of collective modes like charge density waves (CDW) and for spinful fermions also spin density waves (SDW) [21] rather than single particle excitations (particle-hole excitations) as in Fermi liquids.
The life time of an excitation characterizes its stability. The life time for particle hole excitation approaches to zero if it happens closer and closer to the Fermi point in 1d. Thus, particle hole excitations are not stable in 1d and are not a suitable description of excitations.

The particle density expressed in bosonic field ϕ is

$$\rho(x) = (\rho_0 - \frac{1}{\pi}\nabla\phi(x)) \sum_p e^{i2p(\pi\rho_0 x - \phi(x))}. \tag{2.14}$$

A single particle operator can always be written as [21]

$$\psi^\dagger(x) = [\rho(x)]^{1/2} e^{-i\theta(x)}, \tag{2.15}$$

where the density Eq. (2.14) is used and θ is an operator whose physical interpretation becomes clear later.
A generic 1d Hamiltonian should consist of kinetic energy

$$H_{kin} = \int dx \frac{1}{2m}(\nabla\psi^\dagger(x))(\nabla\psi(x))) = \int dx \frac{\rho_0}{2m}(\nabla\theta(x))^2, \tag{2.16}$$

as well as a density density interacting part which is proportional to $\int dx(\nabla\rho)^2(x) \propto \int dx(\nabla\phi(x))^2$. This leads to the most general Hamiltonian describing the low energy (long wavelength) properties of a massless 1d spinless fermionic system [21]

$$H_{LL} = u \int dx(\frac{K}{2}(\nabla\phi)^2 + \frac{1}{2K}(\nabla\theta)^2). \tag{2.17}$$

K is the Luttinger parameter, indicating the nature of the interaction, and u is the plasmon velocity.
The bosonic field spatial derivatives can be interpreted as charge fluctuations $\nabla\phi$ and phase shift (current) $\nabla\theta$, respectively.

A field theoretical approach can be used to describe Luttinger liquids. For this purpose, one changes from Hamiltonian to Lagrangian formalism where the action is the integral over the Lagrangian in imaginary time

$$-S/\hbar = \int_0^\beta d\tau \int dx[\frac{i}{\pi}\nabla\theta(x,\tau)\partial_\tau\phi(x,\tau) - \frac{1}{2\pi}(uK(\nabla\theta(x,\tau))^2 + \frac{u}{K}(\nabla\phi)^2)]. \tag{2.18}$$

Where S is the action and β is inverse temperature. The path integral formalism yields for the partition function

$$Z = \int \mathcal{D}\{\phi,\theta\} e^{-S/\hbar}. \tag{2.19}$$

One can integrate out one of the fields ϕ or θ. This is possible if one Fourier transforms the action Eq. (2.18) and completes the square in the fields. By rescaling and integrating out one of the fields (see Appendix B.1) the action in the field theory formalism is

$$S_\phi = \frac{1}{2\pi K}\int dx \int_0^\beta d\tau \left[\frac{1}{u}(\partial_\tau\phi(x,\tau))^2 + u(\partial_x\phi(x,\tau))^2\right], \tag{2.20}$$

where one can read of the Lagrangian density of the ϕ field

$$\mathcal{L}_\phi = \frac{1}{2\pi K u}\left[(\partial_\tau\phi(x,\tau))^2 + (u\partial_x\phi(x,\tau))^2\right]. \tag{2.21}$$

Finally, we want to arrive at a so called helical Luttinger liquid consisting of right movers with spin up and left movers with spin down (helicity as defined above), or vice versa.

The difference of helical Luttinger liquids to spinless/spinful Luttinger liquids lies in the interaction with magnetic impurities. Backscattering of a helical Luttinger liquid is accompanied by a spin flip if it scatters at an magnetic impurity. Spinless Luttinger liquids do not interact with magnetic impurities and spinful Luttinger liquids do interact with magnetic scatterer, but there is not a constrain such as a spin flip.
This implies that non magnetic impurities can not backscatter a helical Luttinger liquid mode, whereas spinless/spinful Luttinger liquid modes can be backscattered.
The Lagrangian for HLL with two spin-1/2 Kondo impurities is given below in 2.26. It is possible to formally eliminate forward scattering by rescaling fields and changing the Luttinger parameter to an effective one which is done in the Appendix B.2. One can mimic an electron interacting system by changing J_z which is done during the project.
Due to the different scattering possibilities of helical and non-helical Luttinger liquids, different physics can be expected.
If one is interested in low energy physics, the helical edge modes of a 2d Kane Mele system presents a helical Luttinger liquid. This is one reason why the Kane Mele model has been chosen as lattice model during this project. If the system parameters are chosen properly (i.e. non-trivial topological phase, bulk gap is big enough compared to other energy scales), we can assume the helical edge states as helical Luttinger liquid.

2.3 Impurity interactions with conduction electrons

The lattice system will be the Kane Mele lattice that interacts with magnetic impurities. The reason for a specific parameter configuration (i.e. boundary conditions, hoppings etc.) choice will be given in Sect. 3.1.1.
The interaction is between the impurity spin and the bath electron spin via a Kondo type exchange interaction (Sect. 2.3.1).
If one impurity is considered, the system is a standard realization of the Kondo problem (Sect. 2.3.3) where the local moment of the impurity can be screened by the bath electron spins.
If two impurities are considered, they can interact with each other via the itinerant electrons (exchange or RKKY interaction) which is considered in Sect. 2.3.2.
But for two impurities, the Kondo effect can also lead to screened impurity spins (as it is the case in the one impurity model), where the RKKY interaction would be suppressed.
Thus, a competition of both effects exists, first discussed by Doniach [1]. This will be discussed in Sect. 2.3.4.
The peculiarity of helical modes serving as conduction electron bath will be considered in such a way that not all scattering processes are allowed and lead to a changed competition of RKKY and Kondo regimes as for non helical systems (Sect. 2.3.5).

2.3.1 Kondo impurity

A Kondo impurity is attached to the lattice which will be called an add atom in the following (it does not substitute a lattice site of the Kane Mele lattice). This specific configuration is depicted in Fig. 2.5 where no hopping between the lattice site and the impurity site is allowed. The solid line which connects the impurity to the crest site of the lattice marks only the location of the local spin-spin interaction (see Eq. (2.22) below)

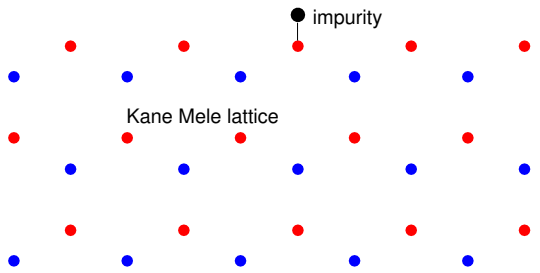

Figure 2.5: Kane Mele lattice with one impurity attached to it. There is no hopping between the lattice and the impurity site, only a spin interaction is allowed (there are no charge fluctuation between lattice and impurity).

The interaction Hamiltonian of an isotropic Kondo impurity is

$$\begin{aligned} H_K &= J\ \vec{s}\ \vec{S}_{imp} \\ &= J \sum_{\sigma\sigma'\tau\tau'} c^\dagger_\sigma \vec{\sigma}_{\sigma\sigma'} c_\sigma f^\dagger_\tau \vec{\tau}_{\tau\tau'} f_\tau, \end{aligned} \tag{2.22}$$

where $\vec{\sigma}$ and $\vec{\tau}$ are the Pauli matrices, $\vec{\sigma} = (\sigma^x, \sigma^y, \sigma^z)$ and $\vec{\tau} = (\tau^x, \tau^y, \tau^z)$. The c operators denote the electron creation and annihilation operators at the Kane Mele lattice where the Kondo impurity is attached. The f operators denote the electron creation and annihilation operators of the impurity. These f operators have to fulfill the constrain that the occupation of the impurity site is 1 (i.e. impurity is always occupied by an up or down particle).

Anisotropy can also be considered, then the Hamiltonian Eq.(2.22) is modified

$$H_K = J_z S^z (c_\uparrow^\dagger c_\uparrow - c_\downarrow^\dagger c_\downarrow) + J_\perp (c_\uparrow^\dagger c_\downarrow S^- + c_\downarrow^\dagger c_\uparrow S^+). \tag{2.23}$$

Here, the abbreviations $S^- = f_\downarrow^\dagger f_\uparrow$, $S^+ = f_\uparrow^\dagger f_\downarrow$ and $S^z = f_\uparrow^\dagger f_\uparrow - f_\downarrow^\dagger f_\downarrow$ are used. An in-plane isotropic Kondo coupling for the J_x and J_y is assumed. It is straightforward to extend the above mentioned Hamiltonians for systems with more Kondo impurities. This implies an additional sum over these impurities with an extra index of the creation and annihilation operators.
If one considers a helical bath, the interaction Hamiltonian Eq. (2.23) has to respect helicity. For such a system spin and propagation direction are in a lock in relation. A backscattered bath electron has to undergo a spin flip of its spin that helicity is conserved. This leads to a spin flip of the impurity spin because of conservation of overall S^z.
With respect to the path integral formalism the impurity problem can be expressed in terms of Lagrangian densities. The Lagrangian densities for forward/backward scattering in a helical Luttinger liquid are

$$\mathcal{L}_{fs} = \frac{iJ_z}{\pi u K} \sum_{j=1,2} \delta(x - x_j) S_j^z \partial_\tau \phi(x, \tau) \tag{2.24}$$

$$\mathcal{L}_{bs} = \frac{J_\perp}{2\pi\alpha} \sum_{j=1,2} \delta(x - x_j) \left[S_j^+ e^{-2i\phi(x,\tau)} + S_j^- e^{+2i\phi(x,\tau)} \right], \tag{2.25}$$

where ϕ is the bosonic field introduced in 2.2 and $S_j^z, S_j^\pm$ are fields describing the degrees of freedom of the Kondo impurity j. α is a UV cut off in form of a lattice constant for example.

The helical nature of the underlying 1d electron bath influences the scattering Lagrangian densities. There is no backscattering of a conduction electron without an impurity spin flip (see Eq. (2.25)) and no spin flip is allowed for forward scattering processes (see Eq. (2.24)).
The full action of the system is

$$S_{tot} = \int dx d\tau \mathcal{L}_{tot} = \int dx d\tau (\mathcal{L}_{bs} + \mathcal{L}_{fs} + \mathcal{L}_{HLL}), \tag{2.26}$$

where τ is the imaginary time and the Lagrangian density of the helical Luttinger liquid $\mathcal{L}_{HLL}$ is defined in Eq. (2.21).

The path integral formalism is used in [2] to tackle the above mentioned two impurities problem in 1d.
An expansion of the backscattering Lagrangian density in $\mathcal{L}_{bs}$ to $J_\perp^2$ order leads to a RKKY interaction description after integration out the bulk bosons.
The bulk bosons in S_{tot} will be integrated out after the expansion, thus only a fermionic theory description of the impurity model remains which is explained in the next section.

2.3.2 RKKY interaction

The Ruderman-Kittel-Kasuya-Yosida (RKKY) interaction is an indirect magnetic exchange interaction. It can be described by a perturbation expansion of the backscattering Lagrangian density in $\mathcal{L}_{bs}$ in the local interaction Kondo coupling constant (see Eq. (2.23)).
Each impurity interacts with an itinerant electron spin (the interaction is local). Those electrons can interact with the other impurity spin. This leads to an effective interimpurity interaction (spin density fluctuation), the RKKY interaction.

The Kondo interaction Hamiltonian up to 2^{nd} order in perturbation theory is (suppress the impurity index convention of Eq. (2.22), now, a capital letter represents the impurity spin)

$$H_{ij}^{(2)} = J\vec{s}\vec{S} - J^2 < (\vec{s}_i\ \vec{S}_i)(\vec{s}_j\ \vec{S}_j) >_{th} |_{\omega=0}. \tag{2.27}$$

The expectation value is defined in 2.43. It is taken over the bath electrons in the static limit $\omega = 0$. The reason for this is that small time differences contribute most [2] which allows a local (in time, i.e. coinciding times) Hamiltonian like in Eq. 2.27.
The second term in Eq. (2.27) is the RKKY interaction Hamiltonian [24]

$$H_{ij}^{RKKY} = \frac{-J^2}{4} \sum_{\alpha\beta\sigma\sigma'} S_i^\alpha \sigma_{\sigma\sigma'}^\alpha \sigma_{\sigma'\sigma}^\beta S_j^\beta \Pi_{ij}^{\sigma\sigma'}(0). \tag{2.28}$$

The S_i^α is the impurity spin operator at site i and $\alpha \in \{x, y, z\}$. The σ^α are the Pauli matrices where $\alpha \in \{x, y, z\}$.
$\Pi_{ij}^{\sigma\sigma'}$ is the conduction electron density propagator between the sites i and j

$$\Pi_{ij}^{\sigma\sigma'}(i\omega) = \frac{-1}{\beta} G_{ij\sigma}(i\epsilon_n + i\omega) G_{ji\sigma'}(i\epsilon_n). \tag{2.29}$$

$G_{ij\sigma}$ is the electron propagator from i to j with spin σ. β is the inverse temperature.
Eq. (2.28) is the RKKY interaction for a general bath.

Now, focusing helical Luttinger liquids serving as bath connected with two anisotropic Kondo impurities, one can describe the system in an effective RKKY regime if perturbative small Kondo coupling is considered [25, 26, 2].
Anisotropy means that forward and backward scattering differs from each other, where J_z is the Kondo coupling which leads to forward scattering (see Eq. 2.24) and $J_\perp$ is the Kondo coupling which leads to backscattering (see Eq. 2.25).
The path integral formalism can be used to integrate out the bath bosonic degrees of freedom (the bosonic ϕ fields in Eq. (2.21)) explained in [21].

The outline of [2] is described here: One can rotate the Lagrangian density $\mathcal{L}_{tot}$ of Eq. (2.26) in the same spirit of what is shown in Appendix B.2 for the Hamiltonian, that one can omit the forward scattering lagrangian density by introducing an effective Luttinger parameter $\tilde{K}$.
Thus, only the backward scattering term and the helical Luttinger bath survive with a modified Luttinger parameter given in Eq. (2.26). One can expand the backscattering part of the action $\exp(-\beta(S_{bs} + S_{HLL}))$ in terms of

$$\int \mathcal{D}\{\text{fields}\}(1 + \frac{\beta^2}{2} S_{bs}^2) \exp(-\beta S_{HLL}),$$

up to second order in $J_\perp$.
The helical Luttinger liquid action S_{HLL} is quadratic in bosonic fields, thus one integrates out the itinerant electrons (or their bosonic counterparts) perturbatively and re-exponentiates the result.

One arrives at an effective action which consists only of the impurity spin degrees of freedom (this is done in [2]). The effective RKKY action is

$$S = -\frac{J_\perp^2}{(2\pi\alpha)^2}\sum_{j,j'}\int d\tau_1 d\tau_2 S_j^+(\tau_1)\Pi(\tau_1-\tau_2)S_{j'}^-(\tau_2), \tag{2.30}$$

where the parameters and the function $\Pi(\tau)$ will be defined below.
If one restricts oneself to $T|\tau_1-\tau_2| \approx |x_j - x_{j'}|/L_T \ll 1$ the action is local in time

$$S_{RKKY} = -E_{RKKY}\int d\tau [S_1^+(\tau)S_2^-(\tau) + S_2^+(\tau)S_1^-(\tau)]. \tag{2.31}$$

This leads to an effective RKKY Hamiltonian which is of $J_\perp^2$ order

$$\hat{H}_{HLL}^{RKKY} = -E_{RKKY}(\hat{S}_1^+\hat{S}_2^- + \hat{S}_2^+\hat{S}_1^-). \tag{2.32}$$

The RKKY energy E_{RKKY} in Eq. (2.32) is

$$\begin{aligned}
E_{RKKY} &= \frac{2J_\perp^2}{(2\pi\alpha)}\int_0^\beta d\tau \Pi(\tau) \\
&= \frac{2J_\perp^2}{(2\pi\alpha)}\int_0^\beta d\tau \left(\left(\frac{\beta u}{\pi\alpha}\right)^2\left[\sin(\pi\tau T)^2 + \sinh(\frac{x_i-x_j}{L_T})^2\right]\right)^{-\tilde{K}} \\
&\propto \frac{J_\perp^2}{u\alpha}\left[\frac{\Gamma(1/2-\tilde{K})}{\Gamma(1-\tilde{K})}\left(\frac{\alpha}{L_T}\right)^{2\tilde{K}-1} + \frac{\Gamma(\tilde{K}-1/2)}{\Gamma(\tilde{K})}\left(\frac{\alpha}{R}\right)^{2\tilde{K}-1}\right] \\
&\propto \frac{\Gamma(\tilde{K}-1/2)}{\Gamma(\tilde{K})}\left(\frac{\alpha}{R}\right)^{2\tilde{K}-1} \quad \text{if} \quad 1/2 < \tilde{K} < 1 \quad \text{and} \quad T \to 0,
\end{aligned} \tag{2.33}$$

where $\Pi(\tau)$ is the bosonic correlator, β is inverse temperature T, τ is imaginary time, u is the renormalized plasmon velocity, $L_T = \beta u/\pi$ is the thermal length and α is a ultra violate cut off (e.g. lattice spacing).
The effective Luttinger parameter in helical Luttinger liquids is (Eq. (B.17))

$$\tilde{K} = K(1 - \frac{J_z}{2\pi u K})^2, \tag{2.34}$$

where one can introduce the density of states $\rho_0 = \pi u$
The effective RKKY Hamiltonian Eq. (2.32) can be used to analyze the system in the RKKY phase. This includes calculations of correlation functions (spectral functions) defined in Appendix B.3.
The Hilbert space of this effective Hamiltonian is (basis $|\beta, i\rangle\langle\alpha, j|$, where the Greek indexes mark the impurity spin (up or down) and the Latin letters specify the impurity location (first or second))

$$H_{RKKY}^{eff} = \begin{pmatrix} 0 & 0 & 0 & 0 \\ 0 & 0 & -E_{RKKY} & 0 \\ 0 & -E_{RKKY} & 0 & 0 \\ 0 & 0 & 0 & 0 \end{pmatrix}. \tag{2.35}$$

The matrix in Eq. (2.35) is diagonalized by the eigenvectors of Hamiltonian Eq. (2.32) which are one singlet and three triplet states. The spectrum is $[\pm E_{RKKY}, 0]$ and the eigenvalue 0 is degenerate. If the RKKY energy is $E_{RKKY} > 0$, the triplet state $\frac{1}{2}(|\uparrow\downarrow\rangle + |\downarrow\uparrow\rangle)$ is the ground state and for negative E_{RKKY} the singlet state is the ground state.

Now, the retarded Greens function can be calculated for the case that the system temperature approaches 0 and the effective RKKY description is valid

$$
\begin{aligned}
G^r_{S_1^z S_2^z}(\omega) &= \int_{-\infty}^{\infty} dt e^{i\omega t - 0^+|t|}(-i)\Theta(t)\langle[\hat{S}_2^z(t), \hat{S}_1^z(0)]\rangle \\
&= \int_0^{\infty} dt e^{i\omega t - 0^+ t}\frac{-i}{Z}\sum_{n,m} e^{-\beta E_n}[e^{i(E_n - E_m)t}\langle n|\,\hat{S}_2^z\,|m\rangle\langle m|\,\hat{S}_1^z\,|n\rangle - \\
&- e^{-i(E_n - E_m)t}\langle n|\,\hat{S}_1^z\,|m\rangle\langle m|\,\hat{S}_2^z\,|n\rangle] \\
&\overset{\mathrm{T}=0}{=} \int_0^{\infty} dt e^{i\omega t - 0^+ t}(-i)\sum_m [e^{i(E_G - E_m)t}\langle G|\,\hat{S}_2^z\,|m\rangle\langle m|\,\hat{S}_1^z\,|G\rangle - \\
&- e^{-i(E_G - E_m)t}\langle G|\,\hat{S}_1^z\,|m\rangle\langle m|\,\hat{S}_2^z\,|G\rangle] \quad \text{assume} \quad E_{RKKY} > 0 \rightarrow |G\rangle = |T\rangle \\
&= \frac{i}{4}\int_0^{\infty} dt e^{i\omega t - 0^+ t}\sum_{m=|S\rangle}[e^{i(E_G - E_m)t} - e^{-i(E_G - E_m)t}] \\
&= \frac{i}{4}\left(\frac{1}{-i(\omega^+ - 2E_{RKKY})} - \frac{1}{-i(\omega^+ + 2E_{RKKY})}\right) \qquad (2.36) \\
&= -\frac{E_{RKKY}}{(\omega^+)^2 - (2E_{RKKY})^2}. \qquad (2.37)
\end{aligned}
$$

Here, the frequency $\omega^+ = \omega + 0^+ i$ is shifted to the upper half plane of the complex plane, $|G\rangle$ is the ground state and E_G the corresponding ground state energy. $\Theta(t)$ is the step function and $[...,...]$ is the commutator. In the third row of Eq. (2.37) zero temperature is assumed, thus only the ground state contributes within the n sum.
Assumed that the RKKY energy is positive, i.e. the triplet state is the ground state, the only non-zero matrix element $\langle G|\,\hat{S}_2^z\,|m\rangle\langle m|\,\hat{S}_1^z\,|G\rangle$ is for $|m\rangle = |S\rangle$ (triplet and singlet states are no eigenvectors of the local impurity spin operators S_i^z) which yields

$$
\langle T|\,\hat{S}_2^z\,|S\rangle\langle S|\,\hat{S}_1^z\,|T\rangle = \langle T|\,\hat{S}_1^z\,|S\rangle\langle S|\,\hat{S}_2^z\,|T\rangle = -\frac{1}{4}. \qquad (2.38)
$$

If one assumes $E_{RKKY} < 0$, the singlet state is the ground state. The calculation can be done in the same way as above, but a global minus sign appears, due to the switched arguments $i(E_G - E_m)t$ in the exponentials of Eq. (2.37) compared to the $E_{RKKY} > 0$ case. This global minus sign cancels itself with the negative sign of E_{RKKY}.
Hence, the interimpurity correlation function for the S^z operators is

$$
G^r_{S_1^z S_2^z}(\omega) = -\frac{|E_{RKKY}|}{(\omega^+)^2 - (2E_{RKKY})^2} \quad E_{RKKY} \in \mathbb{R}, \qquad (2.39)
$$

which is in agreement with the correlator given in [2] Eq. (15).
According to the definition (B.31), the spectral function (2.39) is

$$
\begin{aligned}
A_{S_1^z S_2^z}(\omega) &= -\frac{1}{\pi}\Im(G^r_{S_1^z S_2^z}(\omega)) \\
&= -\frac{1}{\pi}\Im\left(\frac{1}{4}\left(\frac{1}{-(\omega^+ - 2E_{RKKY})} - \frac{1}{-(\omega^+ + 2E_{RKKY})}\right)\right) \\
&= \frac{1}{4\pi}\Im\left(\frac{\omega - 2E_{RKKY} - i0^+}{(\omega - 2E_{RKKY})^2 + (0^+)^2} - \frac{\omega + 2E_{RKKY} - i0^+}{(\omega + 2E_{RKKY})^2 + (0^+)^2}\right) \\
&= \frac{1}{4\pi}\left(\frac{-0^+}{(\omega - 2E_{RKKY})^2 + (0^+)^2} - \frac{-0^+}{(\omega + 2E_{RKKY})^2 + (0^+)^2}\right) \\
&= -\frac{1}{4}\left(\delta(\omega - 2E_{RKKY}) - \delta(\omega + 2E_{RKKY})\right). \qquad (2.40)
\end{aligned}
$$

The spectral function is antisymmetric and is peaked at $\omega = \pm 2E_{RKKY}$ which can be used to calculate the RKKY energy.
Eq. (2.40) fulfills the sum rule (here for $T \to 0$)

$$\int_0^\infty d\omega A_{S_1^z S_2^z}(\omega) = \langle S_1^z S_2^z \rangle = -\frac{1}{4}. \tag{2.41}$$

If one restrict oneself to positive frequencies ω, the interimpurity spectral function is strictly negative deep in the RKKY regime.

The local retarded Green's function of one impurity is

$$G^r_{S_1^z S_1^z}(\omega) = G^r_{S_2^z S_2^z}(\omega) = -G^r_{S_1^z S_2^z}(\omega), \tag{2.42}$$

where the same calculation as above 2.37 can be done.
The crucial difference to the interimpurity retarded correlator given in Eq. (2.37) is the matrix element

$$\langle T| \hat{S}_1^z |S\rangle \langle S| \hat{S}_1^z |T\rangle = 1,$$

which has the opposite sign factor as the correlator in Eq. (2.38) (here, $E_{RKKY} > 0$ which implies that the ground state is the triplet state).
Eq. (2.42) can be used in numerical analysis. If it holds true (i.e. the interimpurity spectral function is the negative counterpart of the local spectral function), it will be a strong indicator that the system is in the RKKY regime. This will be tested in Sect. 3.1.4.

The effective RKKY Hamiltonian at coinciding times allows one to calculate the expectation value for the interimpurity $S_1^z S_2^z$ operators. The triplet state $|T, 0\rangle$ is the ground state, the sum runs offer all states of the Hilbert space
$|m\rangle \in \{|T, 0\rangle, |T, 1\rangle, |T, -1\rangle, |S, 0\rangle\}$ where the T/S denotes triplet/singlet sate, and the number the spin z component) and the RKKY energy is denoted with E_R

$$\begin{aligned}
\langle S_1^z S_2^z \rangle &= \frac{\sum_m \langle m| e^{-\beta \hat{H}} S_1^z \sum_n |n\rangle\langle n| S_2^z |m\rangle}{\sum_m \langle m| e^{-\beta \hat{H}} |m\rangle} && (2.43)\\
&= \frac{2\langle T, -1| S_1^z S_2^z |T, -1\rangle + \langle T, 0| S_1^z S_2^z |T, 0\rangle e^{\beta E_R} + \langle S, 0| S_1^z S_2^z |S, 0\rangle e^{-\beta E_R}}{e^{-\beta E_R} + e^{\beta E_R} + 2} \\
&\to -\frac{1}{4} \quad \text{for} \quad T = 1/\beta \to 0. && (2.44)
\end{aligned}$$

Thus, the expectation value of the interimpurity operator approaches $-1/4$ in the RKKY regime for temperatures which approaches 0.

2.3.3 Kondo effect

The Kondo effect was discovered in experiments measuring the resistivity of noble metals in the 1930s [27]. Before that date, it was commonly accepted that the resistivity of metals decreases if the temperature is lowered. This holds true for many different metals, but not for noble metals like gold or silver. Here, a global minimum of the resistivity exists and the resistivity approaches a finite value for really low energies compared to the so-called Kondo temperature T_K which is defined below (see Fig. 2.6). The Figure shows the Au_3 resistivity dependence on temperature.

The resistivity of metals typically originates from scattering of phonons (lattice vibrations) and impurities or from the lattice umklapp scattering. A T^5 dependence of the resistivity results from phonon scattering and a T^2 contribution follows from the electron-electron interaction which can be explained by Landau's Fermi liquid theory [28].
An explanation of the difference in theory (no minimum) and experiments (minimum) was given by Jun Kondo in 1964. He suggested that the minimum results from a spin-spin interaction between conduction electron spin and a magnetic impurity spin [29].

The Hamiltonian of the Kondo impurity problem is

$$\mathcal{H}_K = \sum_{k\sigma} \epsilon_k c^\dagger_{k\sigma} c_{k\sigma} + J\vec{s}\vec{S}_{imp}, \qquad (2.45)$$

where ϵ_k is a usual quadratic (i.e. non interacting) dispersion relation, the $\vec{S}_{imp}$ is the impurity spin operator, $\vec{s}_c = c^\dagger \vec{\sigma} c$ is the conduction electron spin at the impurity site and $\vec{\sigma}$ are the 3 pauli matrices $\vec{\sigma} = (\sigma^x, \sigma^y, \sigma^z)$. The interaction happens local, thus the involved conduction electron is located nearby the impurity.
The impurity spin results from a localized electron (e.g. the d-orbital of a transition metal) and the conduction electron spin from a s-orbital of a noble metal (e.g. Au). Thus, the above mentioned model is called s-d model or Kondo model.

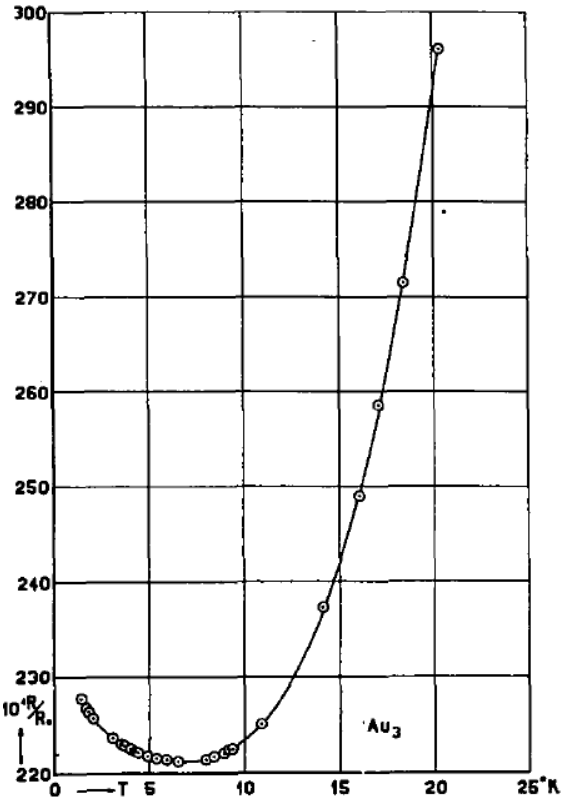

Figure 2.6: Figure copied from [27]. It shows the resistivity minimum of Au_3 in the range of the Kondo temperature. The resistivity is a increasing function for higher temperatures, whereas the resistivity decreases for low energies if the temperature is increased.

There are different methods to attack the single impurity Kondo problem. One can apply perturbation theory in J, this has been done by Anderson and is known as poor man's scaling [30]. It picks up the spirit of RG and predicts an vanishing effective coupling $\tilde{J} \to 0$ for a ferromagnetic coupling $J < 0$ and the strong coupling regime in the antiferromagnetic case.
The second order in perturbation theory results in a logarithmic contribution of the form $J^2 \ln(T/D)$ [31], where J is the coupling constant, T the temperature and D the conduction electron band width. The effects of the RG can be included in an effective coupling constant. If this renormalized coupling constant is of the same order of the first order term of perturbation theory, the perturbation ansatz fails and one approaches the Kondo temperature T_K which can be defined in this way.

Interesting physics happens, if an antiferomagnetic coupling $J > 0$ is considered. There are 2 different energy regimes. The regime where the energy is higher than T_K corresponds to an effective Kondo coupling which is $\tilde{J} = 0$ which implies a non interacting magnetic impurity with the conduction electrons.
The other regime is where energies are smaller than T_K. The effective Kondo coupling explodes $\tilde{J} \to \infty$ called strong coupling limit. Here, the magnetic impurity forms a singlet with one conduction electron spin which effectively quenches the overall spin.

To extract the Kondo temperature one can calculate the $S_1^z S_2^z$ spectral function of the impurity and get the position of the peak. The Kondo temperature is the energy scale which separates energy regimes where physical properties are of conceptual different nature. This can be seen in Sect. 3.1.3 for a single impurity Kondo impurity model. The spectral function is a linear function of frequency for lower/higher energies compared to the Kondo temperature. But the slopes differ and the transformation happens at the Kondo temperature, this can be used as definition of the Kondo temperature (i.e. position of the spectral function maximum).
This is used in Sect. 3.1.3 to calculate the Kondo temperature for the single Kondo impurity model.

2.3.4 Competition of RKKY and Kondo effect

The Kondo effect and RKKY interaction represents two different tendencies of the system to quench the local moments with conduction electrons or by themselves, respectively [32].
The characteristic energy for the Kondo effect is T_K (see Sect. 2.3.3) and E_{RKKY} for the RKKY interaction, see Sect. 2.3.2.

$$T_K \propto \rho_0^{-1} \exp(\frac{-1}{\rho_0 J}) \tag{2.46}$$

$$E_{RKKY} \propto CJ^2\rho_0/R, \tag{2.47}$$

where ρ_0 is the density of conduction electron states, C is a dimensionless constant depending on the band structure and R is the interimpurity distance [1].

For specific parameter settings ($J < J_c$) the RKKY interaction overwhelms the Kondo effect or vice versa ($J > J_c$) which has been investigated by Doniach [1]. The Kondo effect is strong and essentially non-perturbative coupling which can hardly be realized for ordinary systems (e.g. non helical).
The goal of this study is to reach the Kondo regime. The two regimes can be distinguished if one compares their characteristic energy scales which are depicted in Fig. 2.7.
The Kondo effect will overwhelm the RKKY interaction if the Kondo temperature is bigger than the RKKY energy $T_K > E_{RKKY}$ and vice versa for $T_K < E_{RKKY}$.
The RKKY energy and the Kondo temperature will be calculated as explained in previous sections and compared afterwards.
This competition of the different regimes are also examined numerically [33, 34, 35]. In these studies the conduction electrons are non helical. This non-helicity makes the difference between their system and the lattice system which is chosen in this thesis.

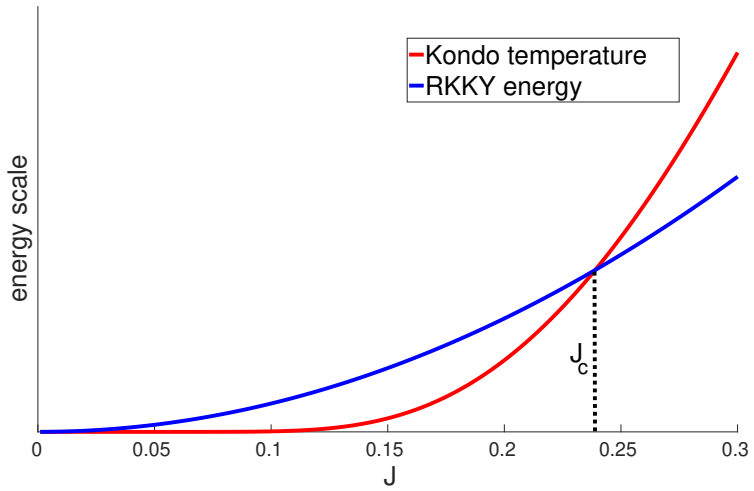

Figure 2.7: Doniach phase's diagram for the competing effects RKKY and Kondo in 1D. The RKKY energy is quadratic in J and the Kondo temperature is $T_K \approx \exp(-1/2\rho_0 J)$. Thus, for Kondo couplings bigger than the quantum critical point J_c the Kondo effect overwhelms the RKKY effect, whereas for small $J's$ the RKKY energy is bigger.

The aforementioned comparison of energy scales will be modified if helical Luttinger liquids are considered due to the scattering process constrains.

2.3.5 Competition of RKKY and Kondo effect in HLL

A system which consists of a helical Luttinger liquid and two Kondo impurities, has another scaling behavior of the RKKY energy and the Kondo temperature compared to a non helical system [2] (see. 2.3.4).
The Kondo temperature has different functional dependencies for different parameter regimes [36]

$$T_K \propto \begin{cases} D\exp(\frac{-1}{\rho_0 J}) & \text{for} \quad 0 < 1-\tilde{K} \ll 1 \quad \text{weak repulsion} \\ D(\rho_0 J_\perp)^{1/(1-\tilde{K})} & \text{for} \quad 1-\tilde{K} \gg \rho_0 J_\perp \quad \text{strong repulsion} \end{cases} . \tag{2.48}$$

$\tilde{K}$ is the effective Luttinger parameter defined in Eq. (B.17) where forward scattering J_z is included. D is the bandwidth, ρ_0 is the density of states at the Fermi level.
The Kondo temperature dependence can be separated into two different repulsive interaction regimes (strong and weak interactions). Their conditions are given in the equation above.
Eq. 2.48 is verified in Sect. 3.1.3 for a single Kondo impurity model. There are 3 possibilities for our set up (obligatory non-interacting bath $K = 1$):
(1) Investigate the weak repulsion regime for isotropic Kondo coupling
(2) Study the strong repulsion regime for anisotropic Kondo coupling for fixed and perturbation small $J_\perp$
(3) Study the strong repulsion regime for anisotropic Kondo coupling for fixed J_z to confirm the power law (Eq. (2.48)) in $J_\perp$
These calculations are done in Sect. 3.1.3. For strong repulsive interaction one sees from Eq. (2.48) that the Kondo temperature T_K is enhanced by the effective interaction $\tilde{K}$.
Thus, the Kondo temperature can be increased by changing the Luttinger parameter K (which is not possible in this setup) or by introducing anisotropy ($J_z \gg J_\perp$), which leads to a change of the effective Luttinger parameter $\tilde{K}$.
The RKKY energy scales like (from Eq. 2.33)

$$E_{RKKY} \propto D(\rho_0 J_\perp)^2 (\alpha/R)^{2\tilde{K}-1} \quad 1/2 < \tilde{K} \leqslant 1. \tag{2.49}$$

R is the interimpurity distance.
The RKKY energy can be calculated via Eq. (2.40) which is done in Sect. 3.1.4.
Now, it is possible to compare the two characteristic energy scales T_K for the Kondo effect in helical Luttinger liquids (Eq. (2.48)) and E_{RKKY} (Eq. (2.49)) which is done in Sect. 3.1.4 numerically for a real lattice system.

In Fig. 1.1 the RKKY/Kondo regimes are depicted. They are separated by the condition $\tilde{K} = 1/2$. The paradigmatic RKKY description fails for strong correlated systems $\tilde{K} < 1/2$. In such a system one will expect two Kondo screened singlets [2]. The system is in the RKKY phase for weak repulsive interactions $\tilde{K} > 1/2$.
The phase diagram suggests two conceptually different possibilities to change the dominant regime. One can changes the interacting parameter K or one can vary the anisotropic Kondo coupling in terms of J_z.
The next sections introduces the concept of numerical renormalization method.

2.4 Numerical Renormalization Group (NRG)

For tackling the aforementioned impurity problem (e.g. Kondo impurities interacting with a bath), the numerical renormalization group (NRG) method is used. NRG is based on the seminal work of Wilson who discovered the usefulness of renormalization group (RG) theory [37] to solve impurity problems non-perturbative.
In this project, the NRG code written by Seung-Sup B. Lee [38, 39] is used, which implements the full-density-matrix NRG [40] by using tensor networks [41, 42].
The gain of NRG in terms of the Kondo problem is a non-perturbation description of the full crossover from a free spin at high temperatures to a screened spin (for the single Kondo impurity model) at low temperatures compared to the Kondo temperature T_K [43].
An impurity with only few degrees of freedom (e.g. spin-1/2 impurity contains only two states) couples to a non-interacting bath (e.g. spinful fermionic system) where symmetries can be used to reduce the computational costs.
The Kondo impurities interact with the conduction electron nearby the impurity, i.e. the local density of states (LDoS) at the Kondo impurities. The occupation of the impurity is fixed. Thus, no charge fluctuations appear at the Kondo impurity site. The allowed interactions between conduction electrons and impurities are only mediated by spin-spin interactions.
The continuum bath is discretized in energy space with a logarithmically chosen grid. If ω_c is the maximum of the conduction band energy, the grid (positive part) can be constructed as follows:

$$[\Lambda^{-(n+1)}\omega_c, \Lambda^{-n}\omega_c] \quad \text{intervals, where} \quad n \in \mathbb{N}_0, \tag{2.50}$$

with $\Lambda > 1$ determining the the discretization.
The width of the intervals decreases exponentially with increasing n. Thus, the resolution of the discretized bath is coarse for high energies but becomes better and better if n increases (i.e. for low energies). This is one of the main advantages of the logarithmic discretization scheme. Since the excitations are expected nearby the Fermi surface, these states will contribute most. Thus, a better resolution of these energetically low states is desirable.
The logarithmic discretization suits problems where no universal energy ranges exist which describes the overall system physics. The Kondo problem is such a problem.
Its perturbation expansion results in logarithmic terms which signals that all energy scales contribute equally to the final result [31]. Hence, no energy range is a priori extraordinary compared to other energy scales and thus all energy scales should be considered.
The logarithmic discretization considers this lack of an outstanding energy scale, it considers every interval equally.
In the logarithmic discretization scheme an easy truncation procedure is conveniently during the iterative diagonalization procedure.
This coarse graining is followed by an exact mapping onto a semi infinite Wilson chain [37, 43]. Its hopping amplitudes decay exponentially. This introduces energy scale separation and thus justifies iterative diagonalization of the Wilson chain.

Based on the argument of energy scale separation by logarithmic discretization, the NRG algorithm proceeds with iterative diagonalization of the Wilson chain. This generates a complete set of well approximated energy eigenstates [38].
The spectral function calculated during this project is [38]

$$\begin{aligned} A_{O_1O_2}(\omega) = &\sum_{E_1,E_2} \delta(\omega - E_2 + E_1) \\ &\times \left(\langle E_1 | \hat{O}_1 | E_2 \rangle \langle E_2 | \hat{O}_2^\dagger \hat{\rho} | E_1 \rangle - \langle E_1 | \hat{O}_1 | E_2 \rangle \langle E_2 | \hat{\rho} \hat{O}_2^\dagger | E_1 \rangle \right). \end{aligned} \tag{2.51}$$

$\hat{\rho}$ is the thermal density matrix, $|E_1\rangle$ and $|E_2\rangle$ are full density matrix eigenstates obtained by iterative diagonalizing the Wilson chain [40] with corresponding energies E_1 and E_2. The spectral function of the operator $\hat{O}_1\hat{O}_2$ is calculated.

Conventional broadening of the discrete spectral density data from NRG calculations is used to improve the resolution of dynamical properties at finite energies. It uses the single width of broadening for all discrete spectral weights.

Chapter 3

Results and discussion

In the following chapter, the results of the numerical analysis are presented. In Sect. 3.1.1, the reason for the choice of specific parameters in the Kane Mele Model that is used in this thesis are given. The local density of states (LDoS) at the edges of the Kane Mele lattice are calculated in Sect. 3.1.2. The Kondo temperature is calculated for a single impurity problem with and without anisotropy in Sect. 3.1.3. In Sect. 3.1.4 two Kondo impurities are considered and RKKY Kondo competition is studied.

3.1 Numerical results

The numerical goal is to investigate the RKKY/Kondo transition in a standard lattice model of the TI. To perform this task, the interimpurity $\langle S_1^z S_2^z \rangle$ spectral functions defined in B.32 and the local impurity $\langle S_1^z S_1^z \rangle$ spectral function defined in B.33 are calculated. These spectral functions can be used to estimate the RKKY energy and the Kondo temperature discussed in previous sections.
Then, following the arguments of Sect. 2.3.5, one identifies the actual regime (either Kondo or RKKY) for the underlying system by comparing their energy scales which are characteristic for each regime.
With this consideration it is possible to yield a more detailed phase diagram like Fig. 1.1 where the winner of the competition is dependent on J_z and K.
A single Kondo impurity model is considered, where the Kondo temperature can be calculated for this system. If the two Kondo impurity system is in the Kondo regime, the two impurities are essentially screened individually, i.e. they are almost uncorrelated. Thus, the two impurities can be treated as two single Kondo impurities. For this reason it is convenient to compare the Kondo temperature calculated from the single impurity Kondo model (Sect. 3.1.3) with the RKKY energy of the two impurities Kondo problem (Sect. 3.1.4) to confirm Doniachs criterion to distinguish RKKY interaction and Kondo effect.

3.1.1 Finite Kane Mele model

The Kane Mele model is chosen because it can be in a topologically nontrivial state [7] and therefor hosts helical edge states at its boundaries.To have access to the boundary, the Kane Mele lattice model is confined in one spatial direction where open boundary conditions (OBC) are applied. This confinement includes different suitable configurations of the boundary, for example zigzag or armchair.
In the following periodic boundary conditions are applied along the horizontal axis and open boundary conditions are applied along the vertical direction depicted in Fig. 3.2.

The focus of interest in this work is the zigzag boundary configuration of the Kane Mele model (see Fig. 2.3). The penetration depth (Fig. 3.1) on its edge states is smaller than the penetration depth of the armchair boundary configuration edge state which is shown in Fig. 3.3 [44].
The penetration of the edge modes is exponentially suppressed into the bulk which is shown in Fig. 3.1 for a zigzag boundary along the OBC direction. Here, the occupation of each site within the unit cell (Fig. 2.1) is depicted. The first site corresponds to the upper edge and the 80^{th} site corresponds to the lower edge. Machine precision will be reached if the 0 energy mode penetrates into the bulk roughly at the 35^{th} site counting from the boundary.
The sharp peaks in the exponential decrease are an artifact of the difference between crest and trough sites in the same leg (see Fig. 2.3). E.g. for the 4^{th} site the occupation is increased compared to the 3^{th} site but will decay afterwards. This feature occurs for a given sequence of sites. But there is an overall exponential decrease which leads to the commonly accepted averaging over a finite amount of sites perpendicular to the edge (a possible averaging is over a leg within a unit cell, thus over 2 sites). This feature will become more important by considering the penetration depth of the armchair configuration (see Fig. 3.3).
Due to this exponential decrease, the 2 edge states are well separated, i.e. their overlap is zero.
The penetration depth depends on the spin orbit coupling t_{so} and the spatial width of the system (here, the width is 80 sites (40 legs)) along the OBC.

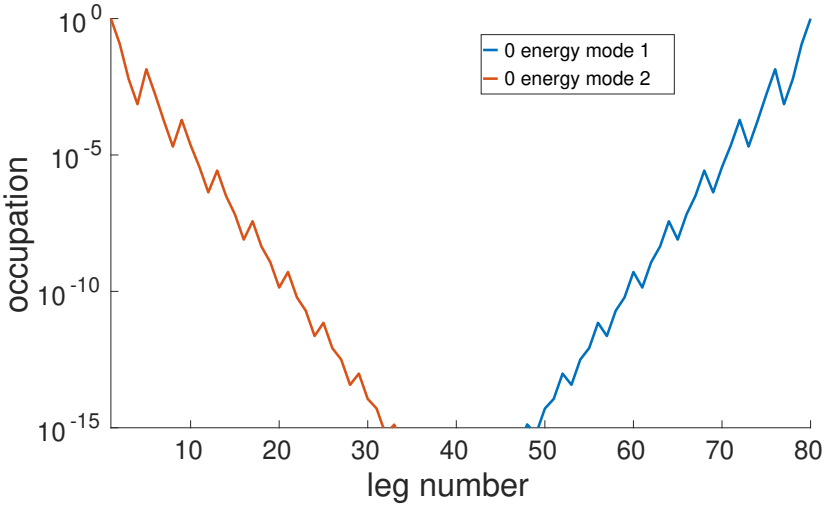

Figure 3.1: This figure depicts the penetration depth of a zero energy mode into the bulk of a Kane Mele lattice where zigzag boundaries are applied. The position of a specific site in the unit cell is marked by the leg number (1 is the upper, 80 is the lower edge). The occupation of these unit cell sites is shown. Here, it is visible that the edge modes decrease exponentially by going into the bulk.

Another possible edge of the honeycomb lattice is the armchair configuration depicted in Fig. 3.2. In this case, a different labeling of sites along the OBC direction is used. One counts layers per-

pendicular to the edge into the bulk (for the zigzag configuration the legs are counted, 2 layers built up 1 leg. However, an enlarged unit cell compared to the zigzag configuration has to be taken into consideration. The unit cell consists of 2 sites per layer. The definition that the spatial upper edge consists of the 1^{st} and the 2^{nd} layer is used within this thesis which will be important by considering the penetration depth into the bulk of the 0 energy states.

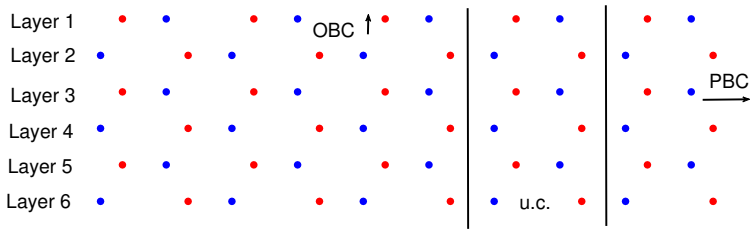

Figure 3.2: Armchair edge along the OBC direction. Here, a different nomenclature is appropriate to label the sites in the unit cell along the OBC direction. 2 layers are 1 leg (nomenclature for the zigzag boundary). It is reasonable to interpret the first two layers of each boundary as the edge which is important for the penetration depth.

The penetration depth of the 0 energy modes (edge modes) in the armchair configuration is depicted in Fig. 3.3. There are 164 layers along the OBC direction (the amount of layers shall guarantee that the system is in the metallic phase seen below). The occupation of each different layer is plotted. There is an exponential decrease if the edge mode penetrates into the bulk. The same spin orbit coupling is used as for the zigzag configuration $t_{so} = 0.06t$ so that the two results are comparable.
The system size of both configurations is also similar but not exactly equal. The reason for this is the necessity to be in the metallic phase for the armchair configuration (164 layers).

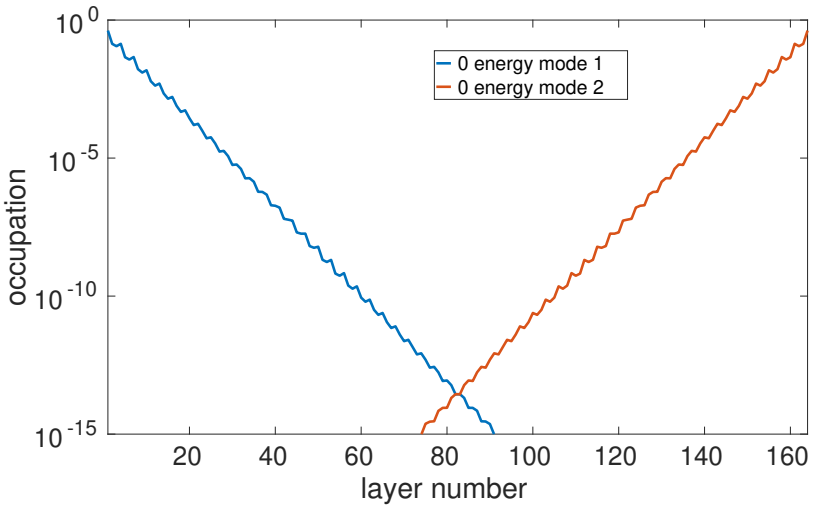

Figure 3.3: This figure depicts the penetration depth of a 0 energy mode for armchair boundary conditions along OBC direction into the bulk. The penetration decreases exponentially. The next nearest neighbor hopping is $t_{so} = 0.06t$. For the armchair boundary the site position in the unit cell are labeled with layers. The figure shows a armchair configuration with 164 layers.

The penetration depth of edge states in the zigzag boundary configuration depicted in Fig. 3.1

decreases faster than the one in the armchair boundary configuration depicted in Fig. 3.3. Thus, one does not need as many lattice sites along the OBC direction for the zigzag configuration as for the armchair configuration for comparable penetration depth (helical edge states are separated). Since we are interested in a model where one spatial dimension is quite small, we exclude the armchair configuration from our considerations.

The armchair configuration is also accompanied by the downside that there are only zero energy modes for a specific amount of sites along the OBC direction [45], which is depicted in Fig. 3.4. A metallic system shows up if the amount of layers along the OBC is $N_y = 3n + 2$ for $n \in \mathbb{N}_0$, otherwise it is gapped. Thus the above chosen system with $N_y = 54 \times 3 + 2 = 164$ is in the metallic phase.
The gap size shrinks with increasing amount of sites along the OBC direction. In the limit $N \to \infty$ the gap is closed. This is reasonable since if one extents the system to infinity, there is no boundary, thus no distinction between armchair and zigzag configuration should appear. The gap size also decreases for increasing amount of layers within the armchair configuration which can be seen in Fig. 3.4. If the system is large (along the OBC direction), it should not change as much by adding one further layer to it as a system which is considerably small. Thus, the gap closing is reasonable. The gap closing for an infinite extended Kane Mele model should be restored.

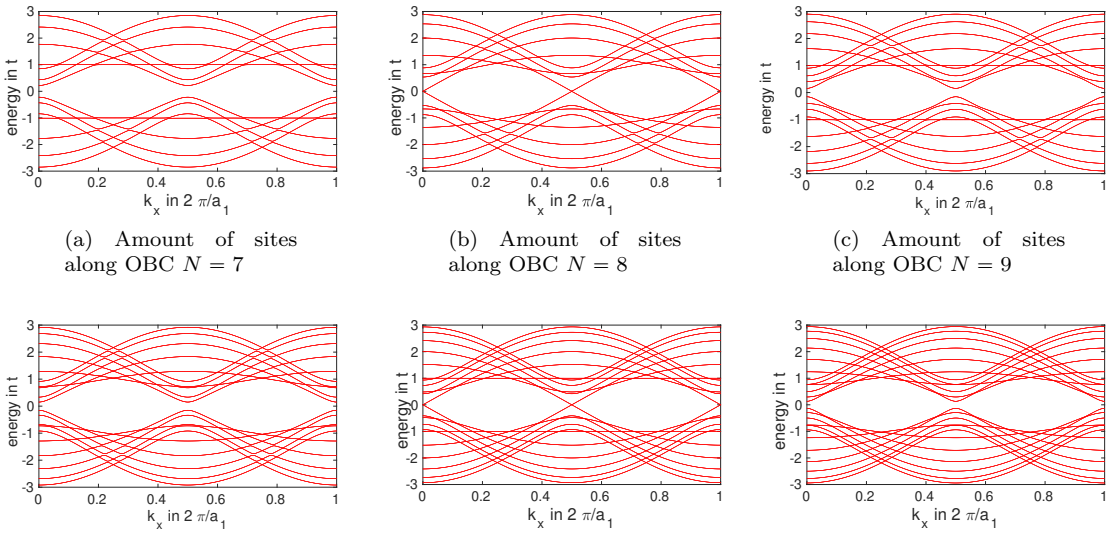

(a) Amount of sites along OBC $N = 7$

(b) Amount of sites along OBC $N = 8$

(c) Amount of sites along OBC $N = 9$

(d) Amount of sites along OBC $N = 10$

(e) Amount of sites along OBC $N = 11$

(f) Amount of sites along OBC $N = 12$

Figure 3.4: Dispersion relation for armchair edge configuration for different amount of legs. There are only metallic configurations in (b) and (e), the others (a)(c)(d)(f) are gapped. The gap shrinks by increasing leg number and approaches 0 if one takes the limit $N \to \infty$.

The zigzag configuration is characterized by the leg number (legs are parallel to the x axis) and the amount of sites along the x direction (for quantization of quasi impulse) which is depicted in Fig. 2.3.

The unit cell of this system consists of two sites per leg. The amount of sites has to be even along PBC as every site from sublattice A has to have a neighboring site from sublattice B. This condition will not be fulfilled if the amount of sites along PBC are odd. This would lead to a term where two sites from the same sublattice are nearest neighbors.

There is a distinction if the dispersion for N is odd or even. This difference appears in the location of the helical states. For odd N, the helical edge states are located at one specific edge depending on its spin which is expected. If N is even, one helical edge state is located at both edges by exactly one half occupation [46]. At first glance, this sounds like a contradiction as helicity should be fixed for each edge mode. However, the edge state which is supported on both edges can fulfill this constraint. Helicity is the signum of group velocity and spin. Thus, the constraint is fulfilled if the edge state part which lives on the upper edge has a different group velocity to the group velocity of the edge state part which lives on the opposite edge (the specific edge state has the same spin).
This half occupation of the boundary for one single helical edge mode can be explained by the geometrical structure of a system consisting of an even amount of legs. For N being even, the boundary consists of different sublattice sites, whereas the edges are constructed from lattice sites which are from the same sublattice for the N being odd case.
In the N being even case there are exact 0 energy modes only in the limit of $N_x \to \infty$ which means that the energy level spacing approaches to 0 [46].

There are 4 exact zero energy modes (helical edge states) in the N being odd configuration independent of the amount of sites along the PBC direction. The degenerated states can be labeled by spin and edge (or by helicity and spin).
The quadratic Kane Mele model can be Fourier transformed and diagonalized. The Fourier transformation is done in Appendix A.1 and results in the matrix which is given in Appendix A.13 which has to be diagonalized. This can be done easily because it is hermitian and has only 1 diagonal and 4 off-diagonal terms. One gets $2N_y$ eigenenergies for each quasi impulse k_x (amount of k_x is dependent on $N_x/2$ sites along open boundary direction). Thus, the dispersion relation consists of $2 \times N_y$ bands and there are exactly the same number of valence band states as conduction band states below and above the Fermi level.
A sublattice potential lifts the spin degeneracy of the dispersion relation. Fig. 2.4 shows the dispersion relations of the Kane Mele model without sublattice potential and with a sublattice potential.
We have come to the conclusion that the following set of parameters will be optimal for the numerical study of the finite Kane Mele lattice: Spin orbit coupling of $t_{so} = 0.03t$, sublattice potential of $\mu = 0$, amount of sites along PBC direction ($M = 500$), amount of legs along OBC $N = 11$ (odd configuration).

The Kane Mele model Eq. (2.11) can be described with spatial (x,y lattice site position) and spin quantum numbers. The Kane Mele Hamiltonian is diagonalized to get the eigen spectrum and eigen vectors of it. The specific chosen basis and labeling of the lattice sites is explained in Appendix A.2). This allows the calculation of specific observables (i.e. the local density of states which is explained below) within a real space resolution.
The treatment (Fourier transformation along one spatial direction) of the Kane Mele Hamiltonian described above is only needed to describe properties of the system without impurities.
The technical procedure for real space quantum number description of the Kane Mele model is explained in Appendix A.2. Each lattice site has to be labeled and a suitable basis in real space has to be chosen (Kane Mele is diagonal in spin). Here, a matrix is generated which has the size of the spatial dimensions $N_x \times N_y$, where the spins are suppressed for the moment.
One is free to choose OBC or PBC (along the x direction) as k_x does not need to be a good quantum number anymore.
This generated matrix can be diagonalized and one is able to use the eigenenergies and eigen states of this system to compute the local density of states which is described in the next section.
Here, one is limited to a smaller system size (e.g. amount of legs is $N = 11$, amount of sites along PBC is 500 yields a Hamiltonian with a dimension of $\dim(H_{KM}) = 5500$).

3.1.2 Local density of states

The Kondo impurity interacts with conduction electrons at the site, where the Kondo impurity is attached Eq. (2.22) (see Fig. 2.5). The local density of conduction electron states at this site is needed for further calculations (i.e. NRG method to solve impurity problems).
The LDoS is defined as

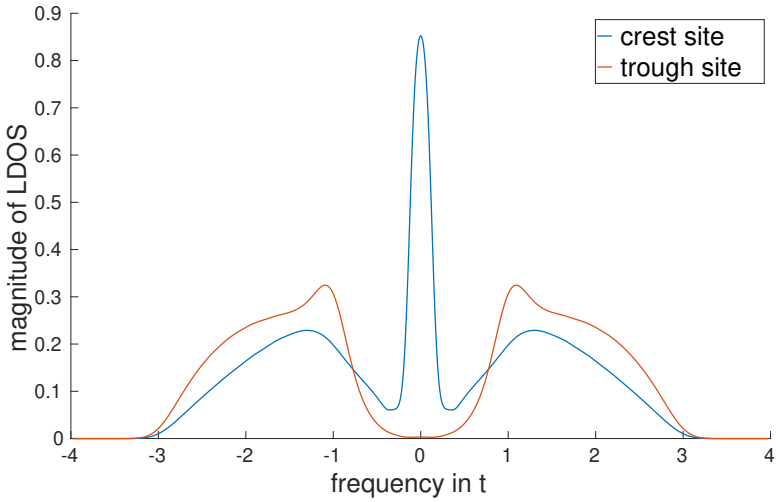

Figure 3.5: The local density of states (LDoS) for different positions on the edge (crest or trough). In the vicinity of the Fermi energy (around 0 frequency) the LDoS is suppressed for the trough site and peaked for the crest site.

$$\Delta_i^D(\omega') = \sum_n \langle i|\epsilon_n\rangle\langle\epsilon_n|i\rangle\,\delta(\omega'-\epsilon_n) = \sum_n W^D(\epsilon_n)\delta(\omega'-\epsilon_n), \tag{3.1}$$

$|\epsilon_n\rangle$ is an eigen state of the Kane Mele Hamiltonian with corresponding eigenenergy ϵ_n. $|i\rangle$ marks the state for which the LDoS is calculated; the state has its position and spin as its quantum number.
We are interested in the local density of states (LDoS) at the boundary of the Kane Mele lattice. There are only two different LDoS for the boundary of this lattice type (when PBC are applied) which are depicted in Fig. 3.5. The LDoS is measured at a crest or a trough site (see Fig. 2.3). PBC ensure that each crest/trough site on its one is equivalent to another crest/trough site along the periodic boundary direction as long as the crest/trough site belongs to the same leg (i.e. here it is the edge leg).
The discrete data generated by implementing Eq. (3.1) has to be broadened because the NRG procedure needs a continuous LDoS. This broadening is done by a linear Gaussian broadening kernel

$$B(\omega,\omega') = \frac{1}{\sqrt{\pi}\eta}\exp((\omega-\omega')/\eta)^2), \tag{3.2}$$

where η is the broadening bandwidth, ω is the frequency argument of the broadened function and ω' is the frequency where the discrete weight is located (i.e. position of the Dirac delta function). The broadened LDoS is

$$\Delta_i^B(\omega) = \int d\omega' W^D(\omega')B(\omega,\omega'), \tag{3.3}$$

and will be called LDoS in the following.
The LDoS is peaked at zero energy for the crest site and suppressed for the trough site which can

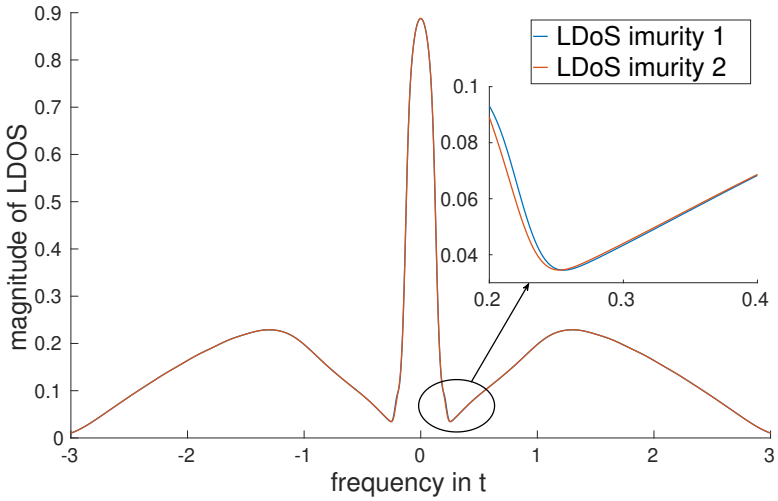

Figure 3.6: LDoS for OBC. The impurities are attached to the boundary; [1,50] and [1,80] in brick stone notation. The Kane Mele lattice consists of 11 legs and 500 sites along the x direction. $t_{so} = 0.03t$ and the nearest neighbor hopping is $t = 1$, $\mu = 0$. There is no obvious difference of the LDoS visible, only by zooming into the figure a noticeable difference can be detected.

be seen in Fig. 3.5. The bulk band gap of the underlying Kane Mele system is in the range of the two local minima ($\Delta_{gap} = t_{so}6\sqrt{3} \approx 0.3t$) of the crest LDoS. The band width is $6t$. This specific lattice system consist of 11 legs (in Appendix A.2 this implies $N_y = 22$ sites within the unit cell) along the OBC direction and 500 sites along the PBC. The nearest neighbor hopping is $t = 1$, the next nearest neighbor hopping is $t_{so} = 0.03t$ and no sublattice potential is turned on $\mu = 0$.

The spatial structure of correlations around a quantum impurity at the edge of a two-dimensional topological insulator is studied in Ref. [47]. The authors also calculated the LDoS for the crest/trough sites at the boundary. Fig. 3.5 shows the LDoS outcome of my calculation which is the same as the result at the crest/trough site at the edge of the Kane Mele lattice given in [47] Fig. 3.

A. Allerdt, A. E. Feiguin, and G. B. Martins choose $t_{so} = 0.1$ to see the finite LDoS of a trough site more clearly at 0 energy.

For OBC along both spatial directions, the LDoS slightly changes compared to the PBC case depicted in Fig. 3.6 if the position along the leg is varied (i.e. 1^{st} crest to 2^{nd} crest along same leg). However, the main feature survives (i.e. crest site LDoS consists of a peak, trough site LDoS is suppressed around the Fermi level).

The parameters are the same as for the PBC case; one spatial direction (along y direction $N = 11$) is significantly not as extended as the other one (amount of sites along horizontal direction $M = 500$). In Fig. 3.6 the LDoS for two impurities attached to two different crest sites along the edge is depicted. One impurity is attached to the 50^{th} site along the edge (blue curve) and the other impurity is attached to the 80^{th} site along the edge (red curve). The inset is a zoom into the region of the bulk gap edge where the difference is most visible.

To consider at the final stage two Kondo impurities attached to the Kane Mele lattice, a more general form as the normal LDoS is needed.

Calculating the interimpurity correlations which is done in Sect. 3.1.3 and Sect. 3.1.4 requires the overlap of eigen states with states located at spatial separate lattice sites $\Delta_{\alpha\beta}(\omega)$ (hybridization). The above mentioned overlap corresponds to a LDoS

$$\Delta_{\alpha\beta}(\omega) = \sum_n \langle\alpha|\epsilon_n\rangle\langle\epsilon_n|\beta\rangle\,\delta(\omega - \epsilon_n), \tag{3.4}$$

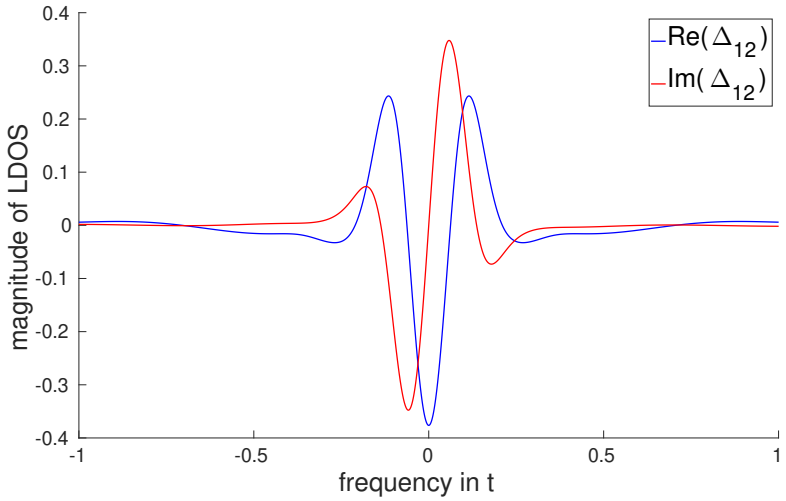

Figure 3.7: Both impurities are attached to crest sites along the edge. The real and imaginary part of the off-diagonal part of Δ from Eq. (3.4) can also be seen. The impurities are separated by 10 lattice sites. The real part of the off-diagonal of Eq. (3.4) is symmetric, the imaginary part is antisymmetric.
System parameters: $t = 1$, $t_{so} = 0.03t$, $\mu = 0$, $M = 500$, $N = 11$ and Impurity position in brick stone notation $Imp_1 = [1, 20]$, $Imp_2 = [1, 30]$ (first entry corresponds to leg number and second entry to the position along the leg).

where $|\epsilon_n\rangle$ are the eigen states with corresponding eigenenergy ϵ_n of the Kane Mele Hamiltonian Eq. (2.11) and the $|\beta\rangle$,$|\alpha\rangle$ are the impurity states.
The diagonal part of Δ is the usual LDoS defined in Eq. (3.1). Δ is a 4×4 matrix and the impurity states are $[|1,\uparrow\rangle, |2,\uparrow\rangle, |1,\downarrow\rangle, |2,\downarrow\rangle]$ where the number marks the impurity (location) and the arrow marks the spin.
The diagonal part of Δ corresponds to the LDoS for each impurity. The off-diagonal part is a hybridization of the local states where the impurities are attached.
There are no spin mixing terms because the Kane Mele Hamiltonian defined in Eq. (2.11) is diagonal in spin space. Thus, Δ is in block diagonal form and it is hermitian which yields, in principal, 6 independent entries.

The off-diagonal part of Δ is generally complex and is depicted in Fig. 3.7. Here, the two impurities will be connected to two crest sites along the same boundary, hence the LDoS for both crest sites will look equal to Fig. 3.5. The first impurity is attached to the 20^{th} site on the outermost leg (first leg) which is noted by $[1, 20]$. The second impurity is attached to the 30^{th} site on the outermost leg (first leg) which is noted by $[1, 30]$, hence the interimpurity distance corresponds to 10 lattice sites.
The real and imaginary part of the hybridization off-diagonal ($\Delta_{1\uparrow,2\uparrow}(\omega)$ or $\Delta_{1\downarrow,2\downarrow}(\omega)$) is symmetric and antisymmetric around 0 energy, respectively.
The visible oscillations within the bulk band gap depend on the interimpurity distance. One oscillation (from 0 energy to the bulk band edge) results from each interimpurity distance change of 8 lattice sites (e.g. the interimpurity distance consists of 10 lattice sites, there is one oscillation). The larger the interimpurity distances the larger the oscillation frequency.

The LDoS for spin up and spin down are equal, but the off-diagonal elements for spin up of Δ are the complex conjugated of the off-diagonal elements of Δ for spin down which can be seen in Fig. 3.8. The reason for this behavior of different spins is the special structure of the Kane Mele Hamiltonian. The two spins are distinguished by a spin orbit term which is $+it_{so}$ for the spin up

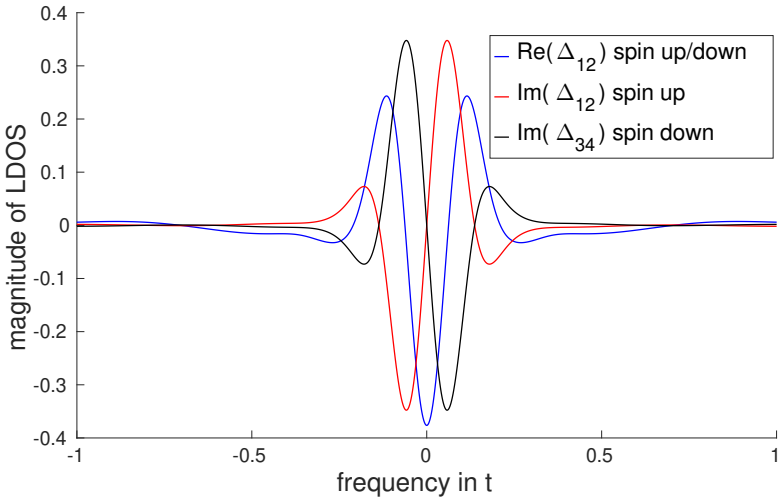

Figure 3.8: The real and imaginary part of the off-diagonal elements for spin up and spin down of the hybridization defined in Eq. (3.4) are depicted here. The real part remains the same for spin up and spin down, but the imaginary part is mirrored around the Fermi level (0 energy). Thus, the off-diagonal elements for spin up and spin down are connected via complex conjugation.

and $-it_{so}$ for the spin down part (see Eq. (2.11)).
The hybridization $\Delta_{\alpha\beta}(\omega)$ is used for the logarithmic discretization procedure which is within the calculation of the Wilson chain hopping's and on-site energies.

3.1.3 Single impurity Kondo model

Only one Kondo impurity is considered in this subsection. The LDoS calculated introduced in the previous section is needed. The impurity site is attached to the crest site of leg number 1 (i.e. at the boundary) like in Fig. 2.5. LDoS is peaked at zero energy and decreases if one goes to higher energies until the energy is of the same order of the bulk gap. Then, the LDoS increases again (see Sect. 3.1.2).

The eigenenergies which are calculated by the NRG iterative diagonalized of the Wilson chain explained in Sect. 2.4 are depicted in Fig. 3.9.
A non stable behavior of the rescaled eigenenergies can be detected in a range of high energies ($n \in [1;35]$) and a stable fix point is reached after chain site 40 (the discretization parameter is $\Lambda = 2$). The degeneracies in energy (marked by numbers near the plotted lines) of the approximate many body eigenstates are typical for a Fermi liquid if the fixed point is reached.
The impurity forms a singlet with the first site of the Wilson chain. The remaining Wilson chain is effectively decoupled from this singlet. Each Wilson chain site can be occupied by 4 different states (empty, 1 particle spin up/down, 2 particles). For an even Wilson chain length the Fermi level is between the ground state and the first exited state. In the Fermi liquid picture, excitations are described by particle hole excitations. Hence, the many body ground state is unique for the even configuration (upper figure).
The Fermi level is at the ground state level for an odd Wilson chain length, hence the ground state is degenerate. There are 4 different states which can occupy the first Wilson chain site, hence the ground state is fourfold degenerate.
This is the ordinary even/odd behavior of the Wilson chain, but the physical content is the same. Strictly speaking, the fixed point Hamiltonian is only a fixed point Hamiltonian of the double

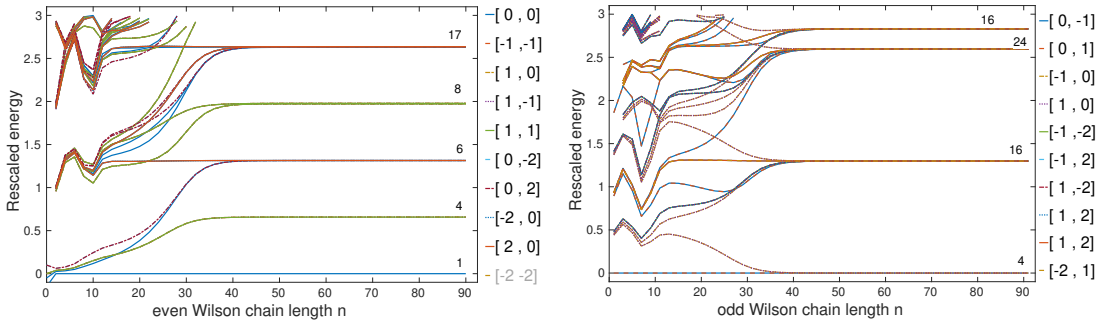

(a) Rescaled energy flow for even Wilson chain length n

(b) Rescaled energy flow for odd Wilson chain length n

Figure 3.9: Energy flow digaram for single impurity Kondo model with anisotropic coupling. For high energies (i.e. low Wilson chain site number) no convergence can be seen. After a specific Wilson chain site the rescaled energies are stable which signals that a fix point is reached. The numbers within the plot near the lines specify the degeneracy of one given many body energy level. The legend shows the quantum numbers which correspond to a given line ([0,1] [charge quantum number, spin z quantum number]). The quantum numbers result from the given system symmetry (ablian charge U(1), and U(1) S_z symmetry)
System parameters: $J_z = 0.4$, $J_\perp = 0.1$, $n_z = 2$, $\lambda = 2$, $N_{keep} = 2000$.

applied renormalization group transformation

$$R(R(H)) \to H.$$

This reflects the antisymmetry between even or odd amount of Wilson chain sites.
The linear spectrum of a Fermi liquid can be seen in the left panel (a) of Fig. 3.9. This suggests that one reaches a Fermi liquid fixed point.
The different lines correspond to different many body states where the quantum numbers for these states are noted in the legend via $[a, b]$.
The system under consideration has 2 symmetries, charge conservation and spin symmetry, which yields a $U(1) \times U(1)$ symmetry. Thus, the quantum numbers, which describe the system, are charge and spin in z direction of the whole system. The charge is measured from half filling. For example the quantum numbers $[1, -1]$ mean that the system consists of one more particle as half filling and the overall spin in z direction is $s_z = -1$. These quantum numbers characterize symmetry sectors. The combined impurity and bath Hamiltonian is in block form with respect to these symmetry sectors.

In such a setup (LDoS + single magnetic impurity), it is possible to calculate the imaginary part of the retarded Greens function (Eq. (B.28)) $\Im(G^r_{S^z S^z}(\omega))$ (i.e. the spectral function) depicted in Fig. 3.10.
The spectral function is antisymmetric, its maximum position is within the range of positive frequencies and corresponds to the Kondo temperature T_K. For energies lower than the Kondo temperature the spectral function linearly depends on the frequency. This behavior corresponds to a Fermi liquid behavior in such an energy range and corresponds to the NRG energy flow depicted in Fig. 3.9 where the fix point Hamiltonian (here a Fermi liquid) is reached.
For frequencies higher than T_K the spectral function decreases linearly.
The Kondo temperature can be calculated by finding the maximum of the spectral function given in Eq. (2.51) in frequency space. In Fig. 3.10 the Kondo temperature is roughly $T_K = \approx 5.7 \times 10^{-7}$, whereas the system temperature is $T = 10^{-12}$.

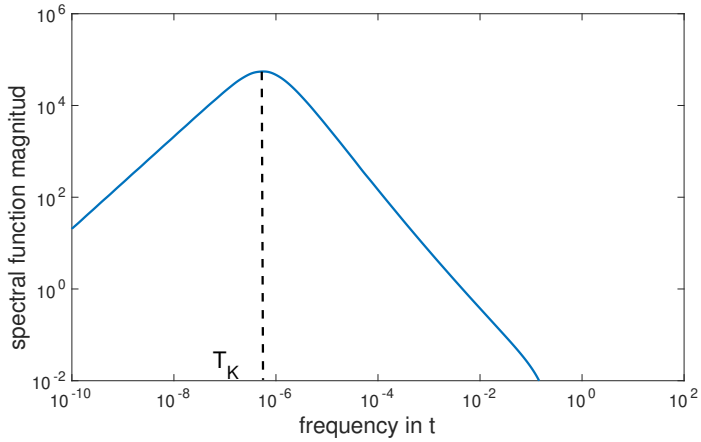

Figure 3.10: The single impurity spectral function for positive energies can be seen in this figure. The isotropic Kondo coupling is $J = 0.1$. The Kondo temperature is at $T_K \approx 5.7 \times 10^{-7}$ which is the spectral function maximum position along the frequency axis. The chosen system temperature is $T = 10^{-12}$.

Fig. 3.11 illustrates spectral functions for different isotropic Kondo couplings $J \in [0.062, 0.1]$. The peak positions of the spectral function in frequency space is shifted to higher energies in that case. This implies that the Kondo temperature increases to higher energies if the Kondo coupling is increased. This figure shows how the Kondo temperature is measured for different couplings.
One can turn ones attention to check that the numerically obtained Kondo temperature agrees with analytically obtained results for the Kondo temperature.
The Kondo temperate is an exponential decaying function of the inverse Kondo coupling for the isotropic single impurity Kondo problem, see in Eq. (2.48). This can be verified numerically. Fig. 3.12 shows a linear fit which confirms that the Kondo temperature depends on the isotropic Kondo coupling J in an exponential way.
The examined Kondo couplings are in the range $J \in [0.07; 0.1]$.
The slope of the fitted curve is

$$\delta \approx 1.2,$$

which is the inverse density of states at the Fermi level

$$\rho_0 \approx 0.83.$$

The value of $\log(T_K)$ where the Kondo coupling obeys $1/J = 0$ is $\log(T_K(\infty)) \approx -2.4$ which leads to the prefactor of the exponential decay

$$\log(D) = -2.4 \rightarrow D = 0.09.$$

D is of the order of the bulk band gap.
Fig. 3.13 shows the power law of the Kondo temperature in $J_\perp \in [0.02; 0.1]$ where $J_z = 0.4$ and $J_z = 0.2$ is fixed for the anisotropic case (see Eq. (2.48)).
The slopes of the fitted curves are the exponent of the power law. The slopes are for the depicted parameter sets

$$\delta \approx 3.2 \quad \text{for} \quad J_z = 0.4$$
$$\delta \approx 5.4 \quad \text{for} \quad J_z = 0.2.$$

The exponent of the power law can be calculated with Eq. (2.48) where the Luttinger parameter has to be replaced by the effective Luttinger parameter $\tilde{K} = K(1 - \rho_0 J_z/2K)^2$ (where $K = 1$)

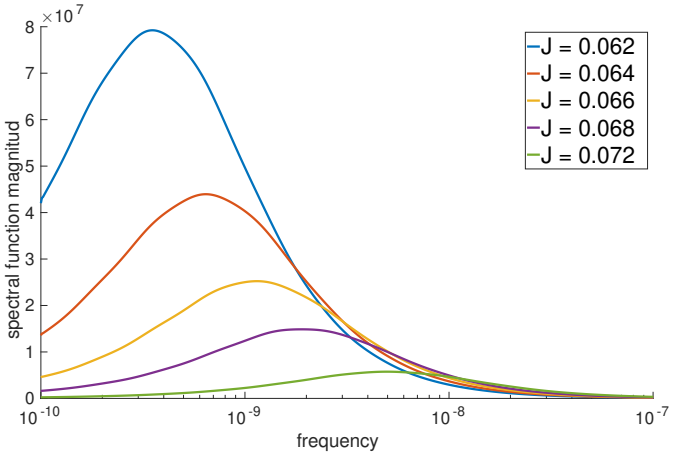

Figure 3.11: The single impurity spectral functions for different isotropic Kondo couplings J are shown in the figure. The Kondo temperature can be extracted from the position of the global maximum of each curve. The main feature is that the maximum of the spectral function shifts to higher energies if the Kondo coupling is increased.

$$1/(1-\tilde{K}) = \frac{1}{1-(1-\rho_0 J_z/2)^2} = \frac{1}{\rho_0 J_z - (\rho_0 J_z)^2/4} \approx \begin{cases} 3.05 & \text{for} \quad J_z = 0.4 \\ 5.82 & \text{for} \quad J_z = 0.2 \end{cases}, \tag{3.5}$$

$\rho_0 = 0.9$ is assumed for the density of states at the Fermi level.

The predicted exponents for the different J_z Kondo couplings fit very well to the numerical obtained ones. The result above confirms the theoretical prediction of the Kondo temperature in a helical quasi 1d system for isotropic and anisotropic Kondo coupling [2].
The attention is now turned to the Kondo temperatures for anisotropic Kondo couplings J_z, whereas $J_\perp = 0.01$ is fixed and perturbatively small. Strong anisotropy enhances the Kondo effect: T_K becomes a power law in $J_\perp$. This leads to an enhanced Kondo temperature, see Eq. (2.48). The system temperature is $T = 10^{-12}$. It should be smaller than the examined Kondo temperature to reach a fixed point in the NRG iteration.
Fig. 3.14 shows the Kondo temperature dependence on the Kondo coupling J_z. The Kondo temperature decreases governed by the dependence given in Eq. (2.48)

$$\log(T_K) \quad \propto \quad 1/(1-\tilde{K})\log(J_\perp) + \log(D) = 1/(J_z - J_z^2/4)\log(J_\perp) + \log(D). \tag{3.6}$$

This behavior is checked in Fig. 3.14(b) for different small $J_\perp \in [0.005; 0.01; 0.02]$.
For lower $J_\perp$ values the equation above is more accurate than for higher ones. The reason for this is the constraint given in Eq. (2.48). This constraint is more satisfied for lower $J_\perp$ as for higher ones.
From Fig. 3.14(a) one can easily read the Kondo temperature for a given parameter set. This will be useful to compare the single Kondo impurity Kondo temperature with the RKKY energy discussed in the next section.

3.1.4 Two Kondo impurities Kondo/RKKY transition in the Kane Mele model

Two Kondo impurities are coupled to the Kane Mele lattice. They interact with the edge modes via a Kondo exchange interaction, see Eq. (2.3.1).

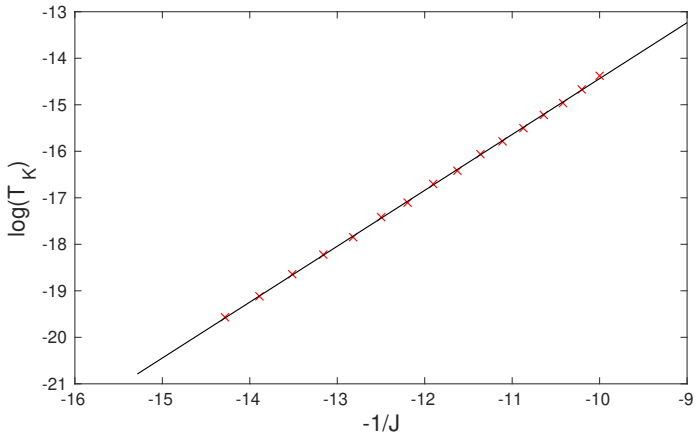

Figure 3.12: The Kondo temperature for isotropic single impurity Kondo coupling. The data points are fitted by a linear fit. The slope is $\delta \approx 1.2$ and $\log(T_K(J=\infty)) \approx -2.4$. This figure confirms $T_K \propto D\exp(-1/J)$ for isotropic coupling.

For handling such problems with NRG, the general hybridization function $\Delta_{\alpha\beta}(\omega)$ discussed in Sect. 3.1.2 and defined in Eq. (3.4) is needed.
The Wilson chain for two impurities has a ladder geometry. There are two spin-1/2 impurities, i.e. two channels, serving as seeds for each ladder leg. Thus, the Hilbert subspace spanned by the impurities is four dimensional. Each site of the Wilson chain has two degrees of freedom; one rung of the ladder consists of for bath sites.
The impurities are coupled to these first bath sites which leads to a Hilbert space dimension of the Hamiltonian consisting of the impurities and the first rung $\dim(H_1) = 2^2 \times 2^4 = 64$.
By attaching one rung to the already existing Wilson ladder, the Hilbert space dimension of the ladder Hamiltonian is $\dim(H_n) = \dim(H_{n-1}) \times 2^4 = 2^2 \times 2^{4n}$. The Wilson chain can be diagonalized, see Sect. 2.4. Below, we will proceed after the following steps:
(1) Study energy flow diagrams
(2) Calculate (interimpurity) spectral functions
(3) Calculate expectation values.

The energy flow diagrams depicted in Fig. 3.15 are more complicated compared to the single Kondo impurity ones. As mentioned above, the Hamiltonian dimension increases faster than for the single impurity Kondo model by going along the Wilson ladder.
The Fermi liquid fix point energy spectrum will be governed by other degeneracies of the many body eigenstates. Those degeneracies are denoted by numbers near the corresponding energy line in the figure.
For this setup the competition of RKKY interaction and the Kondo effect leads to two characteristic energy scales for the system. By studying the energy flow diagrams regions where the characteristic energy scales will occur can be estimated. For the chosen configuration ($J_z = 0.25$, $J_\perp = 0.01$, $\lambda = 8$, $N_{keep} = 4000$, $N_{Wilson} = 45$ and $T = 10^{-16}$) these energy scales are visible. The first one roughly occurs at roughly at $n = 10$ (corresponding energy $\approx 3 \times 10^{-5}$) and the second one at $n = 18$ (corresponding energy $\approx 7.5 \times 10^{-9}$). This energy scales are only an estimation and without a deeper understanding of the system nothing can be said about their nature. At this stage, it can be claimed that there are characteristic energy scales at which physics can change.
Later on, one is able to interpret one of these characteristic energy scales as the RKKY energy if the system is in the RKKY regime (for suitable chosen parameters, i.e. weak anisotropy, see below). If one drives the system away from the RKKY regime by increasing the anisotropy, the characteristic energy scale which was the RKKY energy before is now another energy scale which is not connected with the RKKY regime. However, it describes the underlying physics (starting

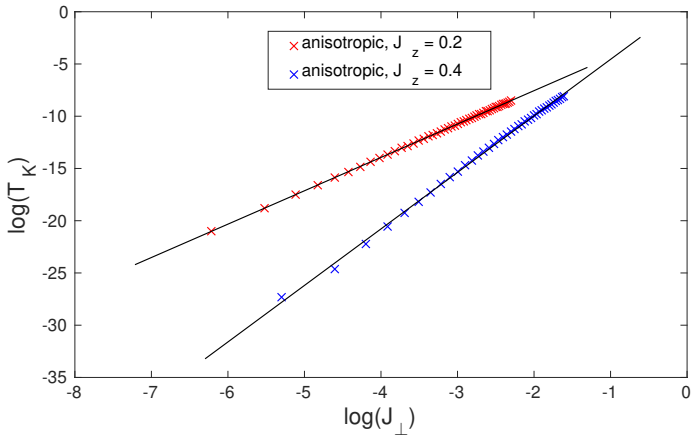

Figure 3.13: Power law of the Kondo temperature versus anisotropic coupling $J_\perp$ with fixed $J_z = 0.4$ (blue) and $J_z = 0.2$ (red). The lines correspond to a linear fit of $\log(T_K)$ and $\log(J_\perp)$. Thus, the slopes $(\approx 3.2)/(\approx 5.4)$ for red/blue yield the exponent of the power law dependence.

from the RKKY phase). This energy will serve as a quasi RKKY energy which can be compared to the Kondo temperature for a single Kondo model.
The fix point in Fig. 3.15 is reached after $n = 25$ Wilson chain sites. The energy spectrum after reaching the fix point Hamiltonian looks like a Fermi liquid one which can be seen from the degeneracies.
The local and non-local (interimpurity) spectral functions are calculated to estimate the RKKY energy. If the system is in the RKKY phase, there is a relation between the local and the interimpurity Green's functions stated in Eq. (2.42). That leads to a connection of the spectral functions (interimpurity and local one)

$$A_{S_1^z S_2^z} = -A_{S_1^z S_1^z}. \tag{3.7}$$

The interimpurity and the local spectral function calculated by using NRG are shown in Fig. 3.16. They obey relation Eq. (3.7) in panel (a). The interimpurity spectral function is negative in the RKKY phase whereas the local one is positive. The peak positions are the same for both spectral functions and are related to the RKKY energy via $\omega_{peak} = 2E_{RKKY}$. The characteristic energy scale for the shown configuration (weak anisotropy) in panel (a) is $E_{RKKY} = 1.3/2 \times 10^{-6}$.
By increasing the anisotropy there should be a qualitative change of the spectral functions, i.e. the spectral functions will not obey Eq. (3.7) any longer which can be seen in Fig. 3.16(b). Here, the peak positions are shifted. The peak for the local spectral function remains quite unchanged whereas the peak position of the interimpurity spectral function appears at an energy scale which is roughly 2 magnitudes smaller than the peak position of the interimpurity spectral function for the weak anisotropic case (panel (a)). This change signals that the system is not in the RKKY regime anymore.

Finally, to identify the regime (either Kondo or RKKY) containing the system, the expectation value of the interimpurity spin z operator $\langle S_1^z S_2^z \rangle$ defined in Eq. (2.43) is calculated.
If the system is in the RKKY regime, it can be described by the effective Hamiltonian at coinciding times Eq. (2.32). The ground state is the triplet (with $m = 0$), see Sect. 2.3.2). The expectation value within the RKKY regime for system temperatures approaching 0 is given by Eq. (2.44)

$$\langle S_1^z S_2^z \rangle \to -1/4 \quad \text{for} \quad T \to 0. \tag{3.8}$$

Eq. 3.8 follows from the sum rule Eq. (2.41). The given expectation value corresponds to the

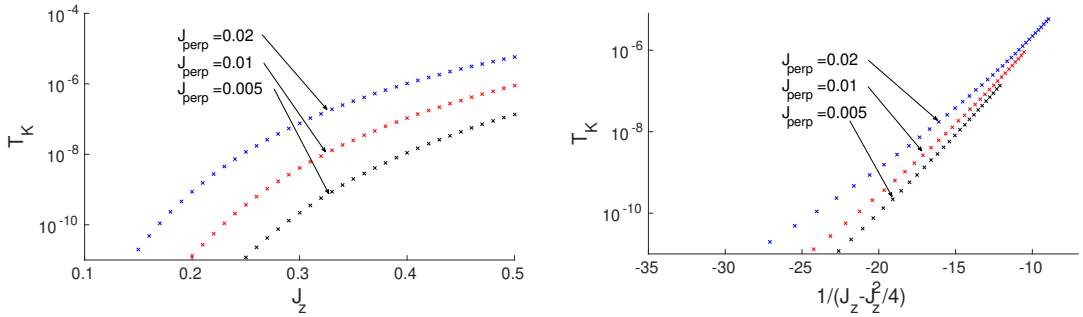

(a) Kondo temperature versus T_K

(b) Confirmation of Eq. (3.6)

Figure 3.14: The Kondo temperature versus the Kondo coupling in z direction (forward scattering) is depicted. In (a) one is able to read the Kondo temperature for specific $J_\perp$ and J_z. (b) shows the numerical confirmation of Eq. (3.6), the curves should be linear until a specific Kondo temperature is reached (smaller but comparable to the system temperature). The equation only holds true in the strong repulsive regime with high anisotropy (i.e. $J_\perp \ll (1-\tilde{K})$).

RKKY regime. It shares the same expectation value as a triplet (singlet) state. The ground state of the RKKY regime is the triplet state.
By changing the parameter sets (increase anisotropy J_z for perturbative small $J_\perp$) one can drive the system into the Kondo phase according to the phase diagram shown in Fig. 1.1.
In the Kondo regime; the interimpurity expectation value approaches 0 (in the low temperature limit).

$$\langle S_1^z S_2^z \rangle \to 0 \quad \text{for} \quad T \to 0. \tag{3.9}$$

This is reasonable since the two Kondo impurities are not related anymore in the Kondo regime they form a Kondo singlet each on its own. Thus, the expectation value decouples in $\langle S_1^z \rangle \langle S_2^z \rangle$ which yields 0, because each expectation value on its own is zero.
The numerical calculated expectation value of the interimpurity operator $\hat{S}_1^z \hat{S}_2^z$ is shown in the lower panel of Fig 3.17. A plot of the expectation values for a wider range of J_z is shown in Appendix A.1.
The upper panel of Fig. 3.17 shows the E_{RKKY}/T_K competition versus anisotropic Kondo coupling J_z (for fixed and small $J_\perp = 0.01$). The RKKY energy (red crosses) overwhelms the Kondo temperature (blue crosses) for small anisotropy (weak repulsive interactions), but at some state ($J_z^{crit} = 0.25$) the Kondo temperature starts to become greater than E_{RKKY} (strong repulsive interactions). The point where the RKKY energy and the Kondo temperature intersect corresponds to Doniach's criterion [1] where both energy scales are of the same order.
The black line corresponds to a polynomial fit of the RKKY energy. Due to a break down of the RKKY regime near the RKKY/Kondo transition, the RKKY energy has to be fitted. Due to this break down, the interimpurity spectral function peak positions for J_z, which are in the vicinity of J_z^{crit}, do not correspond to the RKKY energy any more.
The interimpurity spectral function behaves in a strange way (e.g. sign change) for $J_z > J_z^{crit}$ (not shown in this thesis). This behavior is not clear to us until now (see Sect. 3.3).
The Kondo temperature corresponds to a single Kondo impurity calculation, discussed in Sect. 3.1.3.
The lower panel depicts the expectation value of the interimpurity operator $\hat{S}_1^z \hat{S}_2^z$. The critical Kondo coupling is within the RKKY/Kondo transition region which is explained above.

The RKKY/Kondo transition in HLL is predicted at $\tilde{K} = 1/2$ in [2]. The numerically calculated crossover happens for $J_z = 0.25$ which gives

$$\tilde{K}_n = (1 - J_z \rho_0/2)^2 = 0.7656. \tag{3.10}$$

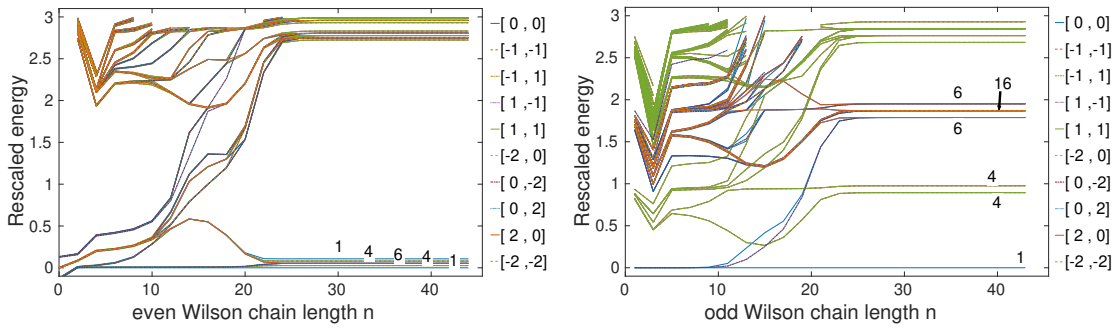

(a) Rescaled energy flow in the two Kondo impurities case for even Wilson chain length n.

(b) Rescaled energy flow in the two Kondo impurities case for odd Wilson chain length n.

Figure 3.15: Energy flow diagram for two Kondo impurities model with anisotropic coupling. Two characteristic energy scales can be seen at Wilson chain site $n = 14$ and $n = 20$. For a chain longer then 25 sites a fixed point Hamiltonian which looks like a Fermi liquid one, is reached. System parameters: $J_z = 0.25$, $J_\perp = 0.01$, $n_z = 1$,$\lambda = 8$,$N_{keep} = 4000$, $N_{Wilson} = 45$, $T = 10^{-16}$.

The numerically found critical effective Luttinger parameter determines the RKKY/Kondo transition line. The difference of the numerically calculated effective Luttinger parameter to the one predicted in [2] can originate from several reasons, which are presented in the following: The investigated models are not the same. In the project at hand a quasi 1d HLL is simulated via the edge states of a TI whereas in [2] a perfect 1d system is used. Within my system the bulk band gap size should be considerably bigger then other system energy scales in the system so that the approximation of the helical edge states is still valid. However, the bulk band gap is always finite. The effective Kondo coupling can only be changed by varying the forward scattering J_z. It is not possible to check J_z^{crit} for other values of K as $K = 1$ has to stay fixed. This corresponds to a line in Fig. 1.1. For other Luttinger parameter values no statement can be made.
The critical effective Luttinger parameter $\tilde{K}_{crit}$ corresponding to the critical forward scattering is bigger in this project compared to [2]. That means that the paradigmatic RKKY descriptions fail for even weaker repulsive interactions than in the analytical calculations of V. Judson and O. Yevtushenko. In my studies, a quite low interimpurity distance is used (10 lattice sites) whereas the aforementioned authors assumed $\alpha \ll R \ll L_T$ which affects their calculations of E_{RKKY}.

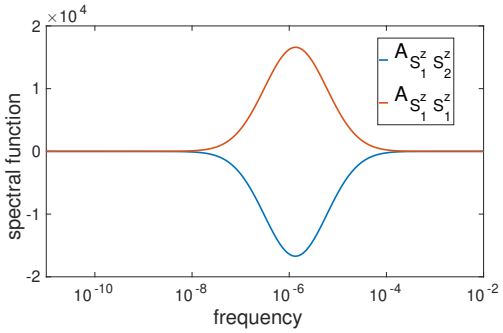

(a) Local and interimpurity spectral functions in the RKKY regime with Kondo couplings $J_\perp = 0.01$ and $J_z = 0.1$

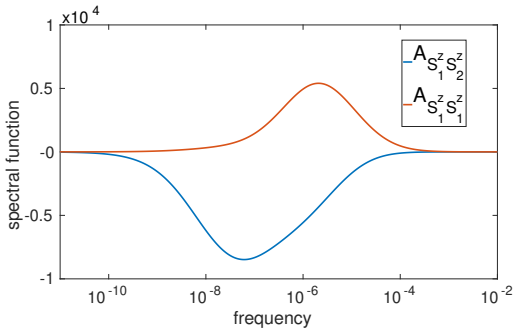

(b) Local and interimpurity spectral functions with Kondo couplings $J_\perp = 0.01$ and $J_z = 0.24$

Figure 3.16: Comparison between inter impurity and local spectral functions calculated for a system which is (a) and is not (b) in the RKKY regime. In panel (a) the spectral functions only differ from each other by an opposite sign factor. Their peak positions are the same. Panel (b) shows the spectral functions behavior (interimpurity/local) for increased anisotropy. Their peak positions are not the same anymore.

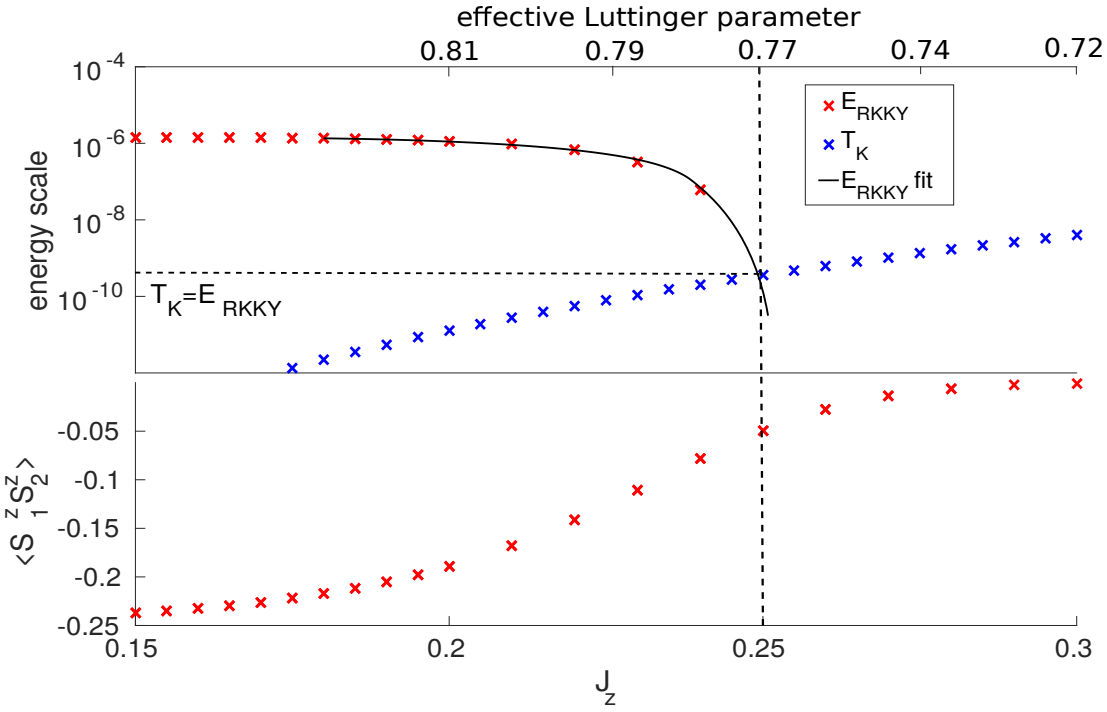

Figure 3.17: Upper panel depicts the comparison of E_{RKKY} and T_K. The lower one shows the exception value of the interimpurity operator versus J_z. Within the weak repulsion regime ($1 > \tilde{K} > 0.77$) the RKKY energy overwhelms the Kondo temperature. The RKKY energy becomes smaller in the strong repulsive regime ($0.77 > \tilde{K} > 0$).

3.2 Conclusions

In this project, I have studied the physics of two Kondo impurities coupled to edges of a QSH sample. The latter has been mimicked with the help of the Kane Mele lattice model.
In the first part of the project, various geometric configurations and system parameters were analyzed in order to find those suitable for the project. The most convincing choice for this lattice model is a boundary consisting of honeycomb zigzag edges. This specific boundary choice ensures that the helical edge states are more confined to the edge than it is the case for the armchair boundary. The edge state for the zigzag configuration supports exact zero energy modes whereas for the armchair configuration the gap is only completely closed in the continuum limit. Thus, their edge states are not exact zero energy modes in a finite system.
Next, properties of a single KI coupled to the Kane Mele lattice have been studied. The single Kondo impurity T_K was calculated where the impurity is attached to the edge of the lattice model mentioned above. The RG predictions for the behavior of T_K in a HLL were confirmed: the exponential dependence of T_K for weak repulsive interactions and the power law dependence of T_K for strong repulsive interactions (i.e. by driving the system into a strong anisotropic regime) given in Eq. (2.48) nicely fit the numerically calculated values.

Finally, the RKKY/Kondo competition in the case of an extremely low impurity density has been investigated. This has been done by considering only two Kondo impurities.
The expected behavior of the interimpurity and local spectral functions deep in the RKKY regime was verified with the help of NRG calculations. The peak position of the minimum of the interimpurity spectral function corresponds with the E_{RKKY}. The RKKY energy can be understood as the energy gap which occurs after the RKKY correlations lift a degeneracy in the energy of the uncorrelated Kondo impurities [2]. If the anisotropy J_z is increased beyond a certain value, this gap will decrease which marks a weakening of the RKKY interaction.
The RKKY interaction overwhelms the Kondo effect for weak anisotropy. However, by increasing the anisotropy J_z the physics are not dominated by the RKKY indirect exchange interaction any longer. The only possible other regime is the Kondo regime where the two magnetic impurities are involved in forming two independent Kondo singlets. This can be explained by Doniach's criterion which states that the RKKY/Kondo transition occurs when the two different characteristic energy scales, the RKKY energy and the Kondo temperature, of both effects become comparable. The numerical results qualitatively fit the analytical theory of Ref. [2]. However, lower anisotropy in comparison to [2] is needed to reach the critical effective Luttinger parameter. The reason for this can be seen in the fact that the Doniach criterion, which is used to estimate the transition region, overestimates the critical coupling [1].
Another possible explanation could be related to different modes used in analytical and numerical approaches.

3.3 Remaining open questions and possible further studies

The first successful study of two Kondo impurities coupled to a Kane Mele lattice model with the help of the NRG paves the way towards various interesting continuations and reveals several important open questions:

- Study of two Kondo impurities coupled to a Kane Mele lattice model for larger interimpurity distances:
  The RKKY energy depends on the interimpurity distance R. From above considerations it can be assumed that one reaches the Kondo regime by separating the two impurities in a great distance from each other. As the Kondo temperature is independent of interimpury distance, the RKKY energy will be smaller than T_K at some critical distance.
- Investigation of the interimpurity spectral function for higher anisotropy than J_z^{crit}:
  - Detailed analysis of the peak position of local spectral function. Until now, do not have any interpretation for it.
  - Detailed analysis of the peak position of interimpurity spectral function. There are more characteristic energy scales upcoming from numerics which we have not understood quit well.
- One can also extend the study to different parameter ranges of the Kane Mele model:
  - Turning on a sublattice potential μ which lifts the spin degeneracy of the Kane Mele model.
  - Varying the next nearest neighbor hopping t_{so} of the Kane Mele lattice model leads to a bigger bulk band gap. However, the next nearest neighbor hopping should not be increased too large compared to the nearest neighbor hopping t. This would destroy the helicity structure of the edge modes.
  - Including Rashba spin orbit coupling allows spin mixing terms within the Kane Mele model.
  - Changing the boundary conditions from the zigzag configuration to the armchair configuration.

Appendices

Appendix A

Numerical supplements

A.1 Fourier transformed Kane Mele in one direction

Here, a zigzag boundary along the open boundary direction is considered. We can Fourier transform the system along the periodic boundary direction. There are N_y sites within the unit cell ($N_y/2$ legs) and N_x unit cells.
The used Fourier transformation of the creation operator is

$$c^{\dagger}_{ij\sigma} = \frac{1}{\sqrt{N_x}} \sum_{k_x}^{N_x} c^{\dagger}_{k_x j\sigma} e^{-ik_x x_i}. \tag{A.1}$$

Here, $k_x \in [0, \frac{2\pi}{a_1}]$ with a step width of $\frac{2\pi}{N_x a_1}$, where $a_1 = \sqrt{3}a$ is the distance of two unit cells and a is the lattice constant. The indexes i and j correspond to the site location in real space in the periodic and the open boundary direction,respectively.
Now, two different cases can appear:
1) Hopping happens within the unit cell and
2) the hopping enters or leaves the unit cell of consideration, which leads to an accumulation of an imaginary phase factor.

Case 1: Hopping within the unit cell (intra unit cell hopping)

$$-t \sum_{<ij>\sigma}^{N_y-1,N_x,2} c^{\dagger}_{ij\sigma} c_{ij+1\sigma} = \frac{-t}{N_x} \sum_{i,k_x,k_x^{'},j,\sigma}^{N_x,N_x,N_x,N_y-1,2} \left(c^{\dagger}_{k_x j\sigma} c_{k_x^{'} j+1\sigma} e^{i(k_x - k_x^{'})x_i} + h.c. \right). \tag{A.2}$$

From now on, I will not assign the summation limits to the sum. The sum over i is a delta function.

$$\frac{1}{N_x} \sum_{i}^{N_x} e^{i(k_x - k_x^{'})x_i} = \delta(k_x - k_x^{'})$$

Thus, this part of the Hamiltonian Eq. (A.2) is

$$H_{NNN/u.c.} = -t \sum_{k_x j\sigma}^{N_y-1} \left(c^{\dagger}_{k_x j\sigma} c_{k_x j+1\sigma} + h.c. \right). \tag{A.3}$$

There is a next nearest neighbor hopping term, which is denoted by $\ll ij \gg$ within the unit cell

$$H_{NNN/u.c.} = -t_{so} i \sum_{\ll ij \gg \sigma\sigma'}^{N_y-2} c^{\dagger}_{ij\sigma} s^{z}_{\sigma\sigma'} c_{i,j+1,\sigma'} = -t_{so} i \sum_{k_x j\sigma\sigma'}^{N_y-2} [(-) c^{\dagger}_{k_x j\sigma} s^{z}_{\sigma\sigma'} c_{k_x j+1\sigma'} + h.c.]. \tag{A.4}$$

Case 2: Inter unit cell hopping
NN hopping: $j/\mathbb{Z}_4$ means i modulo $\mathbb{Z}_4$ and it is diagonal in spin space, thus spin indexes are excluded here

$$\begin{aligned} j/\mathbb{Z}_4 = 1 \rightarrow H_{NN} &= -t\frac{1}{N_x}\sum_{k_x k_x' j}^{N_y-1} c^\dagger_{k_x j+1} c_{k_x' j} e^{i(k_x-k_x')x_i - ik_x a_1} + h.c. \\ &= -t\sum_{k_x j}^{N_y-1} c^\dagger_{k_x j+1} c_{k_x j} e^{-ik_x a_1} + h.c. \\ j/\mathbb{Z}_4 = 3 \rightarrow H_{NN} &= -t\sum_{k_x j}^{N_y-1} c^\dagger_{k_x j+1} c_{k_x j} e^{ik_x a_1} + h.c. \quad . \end{aligned} \tag{A.5}$$

For horizontal NNN hopping:

$$\begin{aligned} j/\mathbb{Z}_2 = 0 \rightarrow H_{NNN/hor} &= -t_{so} i \sum_{\substack{j=even \\ k_x, k_x', \sigma, \sigma'}}^{N_y} [(-) c^\dagger_{k_x,j,\sigma} s^z_{\sigma,\sigma'} c_{k_x',j,\sigma'} e^{ik_x(x_i-a)-k_x' x_i} + h.c.] \\ &= -t_{so} 2 \sum_{\substack{j=even \\ k_x, \sigma, \sigma'}}^{N_y} c^\dagger_{k_x,j,\sigma} s^z_{\sigma,\sigma'} c_{k_x',j,\sigma'} \sin(k_x a_1) \\ j/\mathbb{Z}_2 = 1 \rightarrow H_{NNN/hor} &= -t_{so} 2 \sum_{\substack{j=odd \\ k_x, \sigma, \sigma'}}^{N_y} (-) c^\dagger_{k_x,j,\sigma} s^z_{\sigma,\sigma'} c_{k_x',j,\sigma'} \sin(k_x a_1). \end{aligned} \tag{A.6}$$

The NNN hopping into/out of the unit cell can be distributed in 4 terms, depending on their position in the unit cell:

$$j/\mathbb{Z}_4 = 1 \rightarrow H_{NNN/vert} = -t_{so} i \sum_{k_x,j,\sigma,\sigma'}^{N_y-2} [c^\dagger_{k_x,j+2,\sigma} s^z_{\sigma,\sigma'} c_{k_x,j,\sigma'} e^{-ik_x a_1} + h.c.] \tag{A.7}$$

$$j/\mathbb{Z}_4 = 2 \rightarrow H_{NNN/vert} = -t_{so} i \sum_{k_x,j,\sigma,\sigma'}^{N_y-2} [c^\dagger_{k_x,j+2,\sigma} s^z_{\sigma,\sigma'} c_{k_x,j,\sigma'} e^{ik_x a_1} + h.c.] \tag{A.8}$$

$$j/\mathbb{Z}_4 = 3 \rightarrow H_{NNN/vert} = -t_{so} i \sum_{k_x,j,\sigma,\sigma'}^{N_y-2} [(-) c^\dagger_{k_x,j+2,\sigma} s^z_{\sigma,\sigma'} c_{k_x,j,\sigma'} e^{ik_x a_1} + h.c.] \tag{A.9}$$

$$j/\mathbb{Z}_4 = 0 \rightarrow H_{NNN/vert} = -t_{so} i \sum_{k_x,j,\sigma,\sigma'}^{N_y-2} [(-) c^\dagger_{k_x,j+2,\sigma} s^z_{\sigma,\sigma'} c_{k_x,j,\sigma'} e^{-ik_x a_1} + h.c.]. \tag{A.10}$$

One can also consider a sublattice potential, which is diagonal in real and spin space. It distinguishes A and B sites.

$$j/\mathbb{Z}_2 = 0 \rightarrow H_\mu = -\mu \sum_{k_x,j=even,\sigma}^{N_y} c^\dagger_{k_x,j,\sigma} c_{k_x,j,\sigma} \tag{A.11}$$

$$j/\mathbb{Z}_2 = 1 \rightarrow H_\mu = +\mu \sum_{k_x,j=odd,\sigma}^{N_y} c^\dagger_{k_x,j,\sigma} c_{k_x,j,\sigma}. \tag{A.12}$$

The Kane Mele Hamiltonian Eq. (A.14) can be expressed via the matrix Eq. (A.13) within a suitable basis. This basis consists of states which are of following form $|j,\sigma\rangle(k_x)$. j denotes the

spatial position in the unit cell (along OBC) and σ is, as usual, the spin (e.g. first row corresponds to leg 1 site A, second row to leg 1 site B ...).
Here, only the spin up component is shown, the matrix for the whole system (both spins) is in block diagonal form with respect to spin. For the spin down block, one has to change the next nearest neighbor hopping $t_{so} \to -t_{so}$, whereas all other system parameters have to stay unchanged.

$$H_{\uparrow}^{KM}(k_x) = \begin{pmatrix} A & B-t & C & 0 & 0 & 0 \\ B^*-t & -A & -t & D & 0 & 0 \\ C^* & -t & A & B^*-t & C^* & 0 \\ 0 & D^* & B-t & -A & -t & D^* \\ 0 & 0 & C & -t & A & B-t \\ 0 & 0 & 0 & D & B^*-t & -A \end{pmatrix}, \tag{A.13}$$

with $A = -2t_{so}\sin(k_x a_1)$, $B = -te^{ik_x a_1}$, $C = it_{so}(e^{ik_x a_1} - 1)$ and $D = it_{so}(e^{-ik_x a_1} - 1)$
Thus:

$$\hat{H}^{KM}(k_x) = \sum_{n,m,\sigma} |c^{\dagger}_{n,k_x,\sigma}\rangle H_{\sigma}^{KM}(k_x) \langle c_{m,k_x,\sigma}| \,. \tag{A.14}$$

In principal, the system can be extended to an arbitrary size y by enlarging the unit cell. The diagonal and off-diagonal parts of the above matrix can be continued corresponding to the above "minimal" system (6×6 matrix which corresponds to a system width of 3 legs).
Two different physical situations can occur along the open boundary direction for the conditions $\frac{N_y}{2}/\mathbb{Z}_2 = 1$ and $\frac{N_y}{2}/\mathbb{Z}_2 = 0$. The number of legs $\frac{N_y}{2}$ can be even or odd. This reflects a geometric symmetry distinction. The spatial lattice system is axis symmetric to a parallel to the edge for the even case and inversion symmetric for the odd one.
However, both system configurations will host helical modes on their edges. For $\frac{N_y}{2}/\mathbb{Z}_2 = 1$ there are exact 0 energy modes, whereas for $\frac{N_y}{2}/\mathbb{Z}_2 = 0$ the states which are nearest to the Fermi level will approach to it if one considers more and more sites along the PBC direction, which leads to a shrinking of the inter level spacing of the energies.

A.2 Implementation of real space Kane Mele

The Kane Mele model can also be implemented in real space. This has the advantage that the two impurities can be attached to the Kane Mele lattice in real space. For this, the actual matrix representation of the Kane Mele Hamiltonian is given here.
The used basis consists of states which live on a Hilbert space of the dimension $dim(H) = N*M*2$ amount of legs N, amount of sites along PBC M and 2 spin configurations are possible.
For the nearest neighbor hopping (spin indexes are suppressed here):

$$H_{NN/hor} = -t \sum_{i,j,\sigma}^{N_x,N_y-1} [c^\dagger_{i+1,j,\sigma} c_{i,j,\sigma} + h.c.] \tag{A.15}$$

$$H_{NN/ver} = -t \sum_{i,j,\sigma}^{N_x,N_y-1} [c^\dagger_{i,j+1,\sigma} c_{i,j,\sigma} + h.c.], \tag{A.16}$$

and the next nearest neighbor hopping terms vertical forward $\hookrightarrow$:

$$j = \text{odd}, i = \text{odd} \quad H_{NNN/vert} = -t_{so} i \sum_{i,j,\sigma,\sigma'}^{N_x-1,N_y-1} [(-)c^\dagger_{j-1,i+1,\sigma} s^z_{\sigma,\sigma'} c_{j,i,\sigma'} + h.c.] \tag{A.17}$$

$$j = \text{odd}, i = \text{even} \quad H_{NNN/vert} = -t_{so} i \sum_{i,j,\sigma,\sigma'}^{N_x-1,N_y-1} [(+)c^\dagger_{j-1,i+1,\sigma} s^z_{\sigma,\sigma'} c_{j,i,\sigma'} + h.c.] \tag{A.18}$$

$$j = \text{even}, i = \text{odd} \quad H_{NNN/vert} = -t_{so} i \sum_{i,j,\sigma,\sigma'}^{N_x-1,N_y-1} [(+)c^\dagger_{j-1,i+1,\sigma} s^z_{\sigma,\sigma'} c_{j,i,\sigma'} + h.c.] \tag{A.19}$$

$$j = \text{even}, i = \text{even} \quad H_{NNN/vert} = -t_{so} i \sum_{i,j,\sigma,\sigma'}^{N_x-1,N_y-1} [(-)c^\dagger_{j-1,i+1,\sigma} s^z_{\sigma,\sigma'} c_{j,i,\sigma'} + h.c.], \tag{A.20}$$

and the next nearest neighbor hopping terms vertical backward $\hookleftarrow$:

$$j = \text{odd}, i = \text{odd} \quad H_{NNN/vert} = -t_{so} i \sum_{i>1,j,\sigma,\sigma'}^{N_x,N_y-1} [(+)c^\dagger_{j+1,i-1,\sigma} s^z_{\sigma,\sigma'} c_{i,j,\sigma'} + h.c.] \tag{A.21}$$

$$j = \text{odd}, i = \text{even} \quad H_{NNN/vert} = -t_{so} i \sum_{i>1,j,\sigma,\sigma'}^{N_x,N_y-1} [(-)c^\dagger_{j+1,i-1,\sigma} s^z_{\sigma,\sigma'} c_{i,j,\sigma'} + h.c.] \tag{A.22}$$

$$j = \text{even}, i = \text{odd} \quad H_{NNN/vert} = -t_{so} i \sum_{i>1,j,\sigma,\sigma'}^{N_x,N_y-1} [(-)c^\dagger_{j+1,i-1,\sigma} s^z_{\sigma,\sigma'} c_{i,j,\sigma'} + h.c.] \tag{A.23}$$

$$j = \text{even}, i = \text{even} \quad H_{NNN/vert} = -t_{so} i \sum_{i>1,j,\sigma,\sigma'}^{N_x,N_y-1} [(+)c^\dagger_{j+1,i-1,\sigma} s^z_{\sigma,\sigma'} c_{i,j,\sigma'} + h.c.], \tag{A.24}$$

and the next nearest neighbor hopping terms horizontal:

$$j = \text{odd} \quad H_{NNN/hor} = -t_{so} i \sum_{i,j,\sigma,\sigma'}^{N_x-2,N_y} [(+)c^\dagger_{j+1,i-1,\sigma} s^z_{\sigma,\sigma'} c_{i,j,\sigma'} + h.c.] \tag{A.25}$$

$$j = \text{even} \quad H_{NNN/hor} = -t_{so} i \sum_{i,j,\sigma,\sigma'}^{N_x-2,N_y} [(-)c^\dagger_{j+1,i-1,\sigma} s^z_{\sigma,\sigma'} c_{i,j,\sigma'} + h.c.]. \tag{A.26}$$

The sublattice potential is diagonal in real and spin space, thus easy to implement.
Periodic boundary conditions can also be inserted. This means that the last site in x direction

can for example hop to the first site . This connection of the 2 ends of the Kane Mele model also implies a connection of sites via NNN hopping. Thus, there are some terms which should be included in the Hamiltonian.

A.3 Supplementary figures

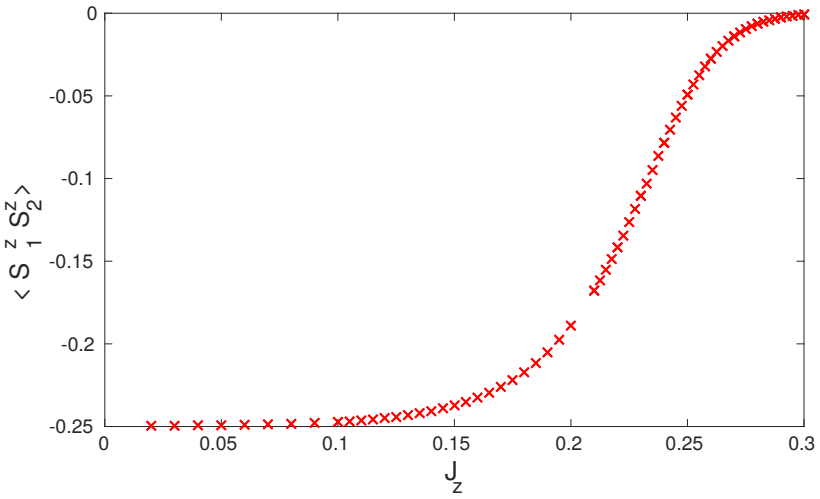

Figure A.1: Expectation value of interimpurity spin z operator $\langle S_1^z S_2^z \rangle$. The range of anisotropic couplings covers the whole transition from RKKY to Kondo regime (i.e. for increasing the J_z the expectation value increases and approaches eventually 0, which is the expected value in the Kondo regime).

Appendix B

Analytical supplements

B.1 Supplementary to Luttinger liquid

This section is devoted to generate a connection between the LL Hamiltonian 2.17 and its corresponding Lagrangian. This step is taken as the Lagrangian is needed for the Feynman field integral formalism, which is a powerful tool to handle many body problems. To do so, it is convenient to Fourier transform Eq.(2.18) with the following definition

$$\phi(x,\tau) = \frac{1}{\beta L}\sum_{q=(\omega_n,k)} \phi(q) e^{ikx - i\tau\omega_n}. \tag{B.1}$$

Thus, the action is

$$-S = \frac{1}{\beta L}\sum_q \left[\frac{-ik\omega_n}{\pi}\phi(q)\theta(-q) - \frac{uK}{2\pi}k^2\theta(q)\theta(-q) - \frac{u}{2\pi K}k^2\phi(q)\phi(-q)\right]. \tag{B.2}$$

For the Fourier transformed fields $\phi^*(q) = \phi(-q)$ and the same for θ. The partition function in field integral formalism

$$Z = \int \mathcal{D}(\phi,\theta) e^{-S}, \tag{B.3}$$

completing the square

$$-S = \frac{1}{\beta L}\sum_q \left[\frac{-\omega_n^2}{2\pi uK}\phi(q)\phi(-q) - \frac{uk^2}{2\pi K}\phi(q)\phi(-q) - \frac{uKk^2}{2\pi}[\theta(q) + \frac{i\omega_n}{uKk}\phi(q)][\theta(q) + \frac{i\omega_n}{uKk}\phi(q)]\right], \tag{B.4}$$

and shifting one field $\tilde{\theta}(q) = \theta(q) + \frac{i\omega_n}{uKk}\phi(q)$ which does not change the measure of the field integration, one can easily integrate out the $\tilde{\theta}$ field

$$Z = Z_\theta \int \mathcal{D}(\phi) \exp\left(\frac{1}{\beta L}\sum_q \frac{-1}{2\pi K}(\frac{\omega_n^2}{u} + uk^2)\phi(q)\phi(-q)\right) \tag{B.5}$$

$$= Z_\theta \int \mathcal{D}(\phi) \exp\left(-\frac{1}{\beta L}\sum_q \mathcal{L}[\phi(q)]\right). \tag{B.6}$$

Fourier transforming back gives the action as a functional depending on ϕ where the field is in imaginary time τ and real space x coordinates basis expressed

$$S_\phi = \frac{1}{\beta L}\sum_q \frac{1}{2\pi K}\left[\frac{\omega_n^2}{u} + uk^2\right]\phi(-q)\phi(q) \tag{B.7}$$

$$= \frac{1}{2\pi K}\int dx \int_0^\beta \left[\frac{1}{u}(\partial_\tau\phi(x,\tau))^2 + u(\partial_x\phi(x,\tau))^2\right]. \tag{B.8}$$

A similar action is the result of a field integration of ϕ. One can proceed as above or simply detect that the Hamiltonian is invariant under $\phi \to \theta$ and $K \to 1/K$. Thus, if this replacements are be done, the corresponding action is

$$S_\theta = \frac{K}{2\theta}\int dx \int_0^\beta \left[\frac{1}{u}(\partial_\tau\theta(x,\tau))^2 + u(\partial_x\theta(x,\tau))^2\right]. \tag{B.9}$$

B.2 Gauge transformation of the helical Luttinger Hamiltonian

The Hamiltonian 2.17 describes an interaction 1d fermionic system. Forward scattering 2.24 can be absorbed into an effective interaction $\tilde{K}$ if one applies a unitary transformation [48, 49, 50]. The Hamiltonian for a helical Luttinger liquid with a magnetic impurity at location 0 is

$$H_{LL} = u \int dx (\frac{K}{2}(\nabla\phi(x))^2 + \frac{1}{2K}(\nabla\theta(x))^2) \tag{B.10}$$

$$H_{bs} = \frac{J_\perp}{2\pi\alpha}\left[S^+ e^{-2i\phi(0)} + S^- e^{+2i\phi(0)}\right] \tag{B.11}$$

$$H_{fs} = -\frac{J_z}{\pi} S^z \partial_x \theta(0). \tag{B.12}$$

H_{LL} is the Luttinger liquid Hamiltonian described and defined in Eq. (2.17). H_{bs} is the backscattering Hamiltonian where the bosonic bath operator picks up a phase shift and the local impurity spin generates a spin flip of the impurity. Here, the helical nature of the underlying bath can be seen. There is no such term which is not helical, e.g. a backscatter process without a spin flip which will also change the helicity of this mode, thus helicity will not be conserved.
H_{fw} is the forward scattering Hamiltonian, where now a spin flip of the impurity spin is forbidden due to the helical nature.

It is convenient for further reason to rescale the bosonic fields $\{\phi, \theta\} \to \{\sqrt{K}\phi', \theta'/\sqrt{K}\}$ which leads to

$$H'_{LL} = \frac{u}{2} \int dx ((\nabla\phi')^2 + (\nabla\theta')^2) \tag{B.13}$$

$$H'_{bs} = \frac{J_\perp}{2\pi\alpha}\left[S^+ e^{-2i\sqrt{K}\phi'} + S^- e^{+2i\sqrt{K}\phi'}\right] \tag{B.14}$$

$$H'_{fs} = -\frac{J_z}{\pi} S^z \partial_x \theta'/\sqrt{K}. \tag{B.15}$$

Apostrophes will be omitted from now on.
Then, a unitary transformation $U = \exp(i\lambda\phi S_z)$ (which is equivalent to an Emery-Kivelson rotation [51]) with $\lambda = \frac{J_z}{u\pi\sqrt{K}}$ is applied to the transformed Hamiltonian

$$U(H_{LL} + H_{bs} + H_{fs})U^\dagger = \tilde{H}_{LL} + \tilde{H}_{bs}, \tag{B.16}$$

where the Luttinger parameter K is replaced by an effective Luttinger parameter

$$\tilde{K} = K(1 - \frac{J_z}{2\pi u K})^2. \tag{B.17}$$

To confirm Eq. (B.16) one can calculate the transformation explicitly.
The canonical commutator relation of the bosonic field is

$$[\partial_x\theta(x), \phi(0)] = -i\pi\delta(x). \tag{B.18}$$

H_{fw} transforms trivially under U, but $UH_{LL}U^\dagger$ obeys an additional term which cancels the forward scattering term and it remains its own form. The backward scattering Hamiltonian changes its phase factor $\pm 2i\sqrt{K} \to \pm 2i\sqrt{\tilde{K}}$.
To see this, one can calculate a part of $H_{LL}U^\dagger$

$$\begin{aligned}\int dx \partial_x\theta(x)[\partial_x\theta(x)\exp(-i\lambda\phi(0))] &= \int dx \partial_x\theta(x)[(-i\pi\delta(x)i\lambda S^z) + \exp(-i\lambda\phi(0))\partial_x\theta(x)] \\ &= (-i2\pi i\lambda S^z)\partial_x\theta(0) + \exp(-i\lambda\phi(0)\int dx(\partial_x\theta(x))^2,\end{aligned} \tag{B.19}$$

which leads to

$$\begin{aligned} UH_{LL}U^\dagger &= U\frac{u}{2\pi}\int dx[(\partial_x\theta(x))^2 + (\partial_x\phi(x))^2]U^\dagger \\ &= H_{LL} + \frac{J_z}{\pi}S^z\partial_x\theta/\sqrt{K}, \end{aligned} \tag{B.20}$$

where the second term is $-H_{fw}$.
The backscattering Hamiltonian changes its phase factor for a spin-1/2 system

$$\begin{aligned} S^+(S_z)^n &= (-1/2)^n S^+ \\ (S_z)^n S^+ &= (1/2)^n S^+, \end{aligned}$$

which can be used for calculating the transformed backscattering Hamiltonian

$$\begin{aligned} \tilde{H}_{bs} = UH_{bs}U^\dagger &= \frac{J_\perp}{2\pi\alpha}\left[e^{-i\lambda\phi S_z}S^+e^{-2i\sqrt{K}\phi}e^{i\lambda\phi S_z} + h.c.\right] \\ &= \frac{J_\perp}{2\pi\alpha}\left[S^+e^{-2i\sqrt{K}(1-\lambda/2)\phi} + h.c.\right]. \end{aligned} \tag{B.21}$$

Thus, the unitary transformation U transforms the original Hamiltonian to Eq. (B.16), where forward scattering is absorbed in the Luttinger Parameter. Forward scattering can be seen as modification of the bath electron Coulomb interaction.
This absorption of H_{fw} only works for helical systems as for backscattering of non helical liquids there is no constraint that the backscattering of an electron is accompanied by a spin flip of the impurity.

B.3 Green functions and spectral functions

Definition of correlator functions (CF)

$$G_\tau(\tau_2-\tau_1) = -T_\tau\langle\hat{B}(\tau_2)\hat{A}(\tau_1)\rangle \quad \text{imaginary time CF} \tag{B.22}$$

$$G_t(t_2-t_1) = -iT_t\langle\hat{B}(t_2)\hat{A}(t_1)\rangle \quad \text{real time CF} \tag{B.23}$$

$$G_r(t_2-t_1) = -i\Theta(t_2-t_1)\langle[\hat{B}(t_2),\hat{A}(t_1)]_\sigma\rangle \quad \text{retarded CF} \tag{B.24}$$

$$G_a(t_2-t_1) = +i\Theta(t_1-t_2)\langle[\hat{B}(t_2),\hat{A}(t_1)]_\sigma\rangle \quad \text{advanced CF,} \tag{B.25}$$

where τ/t is imaginary/real time, T_t/T_τ is the real/imaginary time ordering operator, $\Theta(t)$ is the Heaviside theta function (1 for positive, 0 for negative argument) and $[...,...]_\sigma$ is the commutator/anti commutator for $\sigma = +/-$ (i.e. bosonic/fermionic operators).
Switch from Schrödinger to Heisenberg picture of operators

$$A(\tau) = e^{\tau(\hat{H}-\mu\hat{N})}Ae^{-\tau(\hat{H}-\mu\hat{N})} \tag{B.26}$$

$$A(t) = e^{it(\hat{H}-\mu\hat{N})}Ae^{-it(\hat{H}-\mu\hat{N})}. \tag{B.27}$$

We can express the Green's function using the Lehmann-representation, where $E_n|n\rangle$ is an exact eigenstate of $(\hat{H}-\mu\hat{N})$. Then, the average can be understood as a expectation value $< ... >= \frac{1}{Z}\sum_n e^{-\beta E_n}\langle n|...|n\rangle$, where Z is the partition sum and β inverse temperature.
For instance, the retarded Greens function in frequency space can be calculated as

$$\begin{aligned}
G_r(\omega) &= \int_{-\infty}^{\infty} dt e^{i\omega t-0^+|t|}G_r(t) \\
&= \int_0^{\infty} dt e^{i\omega t-0^+t}\frac{-i}{Z}\sum_{n,m}e^{-\beta E_n}[e^{i(E_n-E_m)t}[\langle n|\hat{B}|m\rangle\langle m|\hat{A}|n\rangle - \\
&- \sigma e^{-i(E_n-E_m)t}\langle n|\hat{A}|m\rangle\langle m|\hat{B}|n\rangle] \\
&= \frac{-i}{Z}\sum_{n,m}e^{-\beta E_n}\left[\frac{\langle n|\hat{B}|m\rangle\langle m|\hat{A}|n\rangle}{-i(\omega+i0^+ + E_n - E_m)} - \sigma\frac{\langle n|\hat{A}|m\rangle\langle m|\hat{B}|n\rangle}{-i(\omega+i0^+ + E_m - E_n)}\right] \\
&= \frac{1}{Z}\sum_{n,m}\frac{e^{-\beta E_n}-\sigma e^{-\beta E_m}}{\omega+i0^+ + E_n - E_m}\langle n|\hat{B}|m\rangle\langle m|\hat{A}|n\rangle.
\end{aligned} \tag{B.28}$$

The last equality sign holds true after renaming the states $|n\rangle$ and $|m\rangle$ in the second expression.
Now, the spectral function, which can be calculated numerically, can be defined as (shift time axis $t_2 = t$ and $t_1 = 0$)

$$A(\omega) = \frac{1}{-2\pi i}(G_r(\omega)-G_a(\omega)) = \frac{1}{-2\pi i}(G_r(\omega)-G_r^\dagger(\omega)) \tag{B.29}$$

$$= \sum_{n,m}\left(e^{-\beta E_n}-\sigma e^{-\beta E_m}\right)\langle n|\hat{B}|m\rangle\langle m|\hat{A}|n\rangle\delta(\omega-E_m+E_n). \tag{B.30}$$

Eq. (B.29) presents the relation between the spectral function and the retarded Green's function. One is able to connect the imaginary part of the retarded Green's function with the spectral density via

$$A(\omega) = -\frac{1}{\pi}\Im(G_r(\omega)). \tag{B.31}$$

The operators $\hat{B} = \hat{S}_1^z$ and $\hat{A} = \hat{S}_2^z$ commute in the considered case, thus $\sigma = +1$ in Eq.(B.29). The calculated quantity is the interimpurity $\hat{S}_1^z, \hat{S}_2^z$ spectral function, defined by

$$A_{S_1^zS_2^z}(\omega) = \sum_{n,m}\left(e^{-\beta E_n}-\sigma e^{-\beta E_m}\right)\langle n|\hat{S}_2^z|m\rangle\langle m|\hat{S}_1^z|n\rangle\delta(\omega-E_m+E_n), \tag{B.32}$$

as well as the local spectral functions $\hat{S}_1^z, \hat{S}_1^z$ and $\hat{S}_2^z, \hat{S}_2^z$

$$A_{S_i^z S_i^z}(\omega) = \sum_{n,m} \left(e^{-\beta E_n} - \sigma e^{-\beta E_m}\right) \langle n| \hat{S}_i^z |m\rangle \langle m| \hat{S}_i^z |n\rangle \, \delta(\omega - E_m + E_n), \tag{B.33}$$

where $i \in [1, 2]$ indicates which impurity is considered.

Bibliography

[1] S. Doniach, "The kondo lattice and weak antiferromagnetism," *Physica B+ C*, vol. 91, pp. 231–234, 1977.

[2] O. M. Yevtushenko and V. I. Yudson, "Kondo impurities coupled to a helical luttinger liquid: Rkky-kondo physics revisited," *Physical review letters*, vol. 120, no. 14, p. 147201, 2018.

[3] X.-L. Qi and S.-C. Zhang, "Topological insulators and superconductors," *Reviews of Modern Physics*, vol. 83, no. 4, p. 1057, 2011.

[4] S. Wolf, D. Awschalom, R. Buhrman, J. Daughton, S. Von Molnar, M. Roukes, A. Y. Chtchelkanova, and D. Treger, "Spintronics: a spin-based electronics vision for the future," *Science*, vol. 294, no. 5546, pp. 1488–1495, 2001.

[5] K. v. Klitzing, G. Dorda, and M. Pepper, "New method for high-accuracy determination of the fine-structure constant based on quantized hall resistance," *Physical Review Letters*, vol. 45, no. 6, p. 494, 1980.

[6] F. D. M. Haldane, "Model for a quantum hall effect without landau levels: Condensed-matter realization of the" parity anomaly"," *Physical Review Letters*, vol. 61, no. 18, p. 2015, 1988.

[7] C. L. Kane and E. J. Mele, "Quantum spin hall effect in graphene," *Physical review letters*, vol. 95, no. 22, p. 226801, 2005.

[8] M. Z. Hasan and C. L. Kane, "Colloquium: Topological insulators," *Reviews of Modern Physics*, vol. 82, no. 4, p. 3045, 2010.

[9] C. L. Kane and E. J. Mele, "Z_2 topological order and the quantum spin hall effect," *Phys. Rev. Lett.*, vol. 95, p. 146802, Sep 2005.

[10] B. A. Bernevig and T. L. Hughes, *Topological insulators and topological superconductors*. Princeton University Press, 2013.

[11] S.-Q. Shen, *Topological insulators*, vol. 174. Springer, 2012.

[12] M. König, S. Wiedmann, C. Brüne, A. Roth, H. Buhmann, L. W. Molenkamp, X.-L. Qi, and S.-C. Zhang, "Quantum spin hall insulator state in hgte quantum wells," *Science*, vol. 318, no. 5851, pp. 766–770, 2007.

[13] A. M. Essin and V. Gurarie, "Bulk-boundary correspondence of topological insulators from their respective green's functions," *Physical Review B*, vol. 84, no. 12, p. 125132, 2011.

[14] A. P. Schnyder, S. Ryu, A. Furusaki, and A. W. Ludwig, "Classification of topological insulators and superconductors in three spatial dimensions," *Physical Review B*, vol. 78, no. 19, p. 195125, 2008.

[15] M. R. Zirnbauer, "Symmetry classes," *arXiv preprint arXiv:1001.0722*, 2010.

[16] K.-I. Imura, S. Mao, A. Yamakage, and Y. Kuramoto, "Flat edge modes of graphene and of z 2 topological insulator," *Nanoscale research letters*, vol. 6, no. 1, p. 358, 2011.

[17] S.-B. Zhang, H.-Z. Lu, and S.-Q. Shen, "Edge states and integer quantum hall effect in topological insulator thin films," *Scientific reports*, vol. 5, p. 13277, 2015.

[18] R. E. Prange and S. M. Girvin, *The Quantum Hall effect, Graduate texts in contemporary physics*, vol. 10. 1987.

[19] X.-L. Qi and S.-C. Zhang, "Topological insulators and superconductors," *Reviews of Modern Physics*, vol. 83, no. 4, p. 1057, 2011.

[20] D. Sheng, Z. Weng, L. Sheng, and F. Haldane, "Quantum spin-hall effect and topologically invariant chern numbers," *Physical review letters*, vol. 97, no. 3, p. 036808, 2006.

[21] T. Giamarchi, *Quantum physics in one dimension*, vol. 121. Oxford university press, 2004.

[22] B. D. Simons and A. Altland, *Condensed Matter Field Theory*. CAMBRIDGE UNIVERSITY PRESS, 2010.

[23] C. Kane and M. P. Fisher, "Transmission through barriers and resonant tunneling in an interacting one-dimensional electron gas," *Physical Review B*, vol. 46, no. 23, p. 15233, 1992.

[24] J. Gao, W. Chen, X. Xie, and F.-c. Zhang, "In-plane noncollinear exchange coupling mediated by helical edge states in quantum spin hall systems," *Physical Review B*, vol. 80, no. 24, p. 241302, 2009.

[25] Y.-W. Lee and Y.-L. Lee, "Electrical control and interaction effects of the rkky interaction in helical liquids," *Physical Review B*, vol. 91, no. 21, p. 214431, 2015.

[26] P. Kurilovich, V. Kurilovich, and I. Burmistrov, "Indirect exchange interaction between magnetic impurities in the two-dimensional topological insulator based on cdte/hgte/cdte quantum wells," *Physical Review B*, vol. 94, no. 15, p. 155408, 2016.

[27] W. De Haas and G. Van den Berg, "The electrical resistance of gold and silver at low temperatures," *Physica*, vol. 3, no. 6, pp. 440–449, 1936.

[28] G. D. Mahan, *Many-particle physics*. Springer Science & Business Media, 2013.

[29] J. Kondo, "Resistance minimum in dilute magnetic alloys," *Progress of theoretical physics*, vol. 32, no. 1, pp. 37–49, 1964.

[30] P. Anderson, "A poor man's derivation of scaling laws for the kondo problem," *Journal of Physics C: Solid State Physics*, vol. 3, no. 12, p. 2436, 1970.

[31] A. C. Hewson, *The Kondo problem to heavy fermions*, vol. 2. Cambridge university press, 1997.

[32] J. Gan, "Solution of the two-impurity kondo model: critical point, fermi-liquid phase, and crossover," *Physical Review B*, vol. 51, no. 13, p. 8287, 1995.

[33] R. M. Fye and J. E. Hirsch, "Quantum monte carlo study of the two-impurity kondo hamiltonian," *Physical Review B*, vol. 40, no. 7, p. 4780, 1989.

[34] B. Jones, C. Varma, and J. Wilkins, "Low-temperature properties of the two-impurity kondo hamiltonian," *Physical review letters*, vol. 61, no. 1, p. 125, 1988.

[35] J. E. Hirsch and R. M. Fye, "Monte carlo method for magnetic impurities in metals," *Physical review letters*, vol. 56, no. 23, p. 2521, 1986.

[36] X.-Y. Feng, J. Dai, C.-H. Chung, and Q. Si, "Competing topological and kondo insulator phases on a honeycomb lattice," *Physical review letters*, vol. 111, no. 1, p. 016402, 2013.

[37] K. G. Wilson, "The renormalization group: Critical phenomena and the kondo problem," *Reviews of modern physics*, vol. 47, no. 4, p. 773, 1975.

[38] S.-S. B. Lee and A. Weichselbaum, "Adaptive broadening to improve spectral resolution in the numerical renormalization group," *Physical Review B*, vol. 94, no. 23, p. 235127, 2016.

[39] S.-S. B. Lee, "Numerical renormalization group (nrg) code package based on the qspace tensor network library.,"

[40] A. Weichselbaum and J. von Delft, "Sum-rule conserving spectral functions from the numerical renormalization group," *Phys. Rev. Lett.*, vol. 99, p. 076402, 2007.

[41] A. Weichselbaum, "Tensor networks and the numerical renormalization group," *Physical Review B*, vol. 86, no. 24, p. 245124, 2012.

[42] A. Weichselbaum, "Non-abelian symmetries in tensor networks: A quantum symmetry space approach," *Annals of Physics*, vol. 327, no. 12, pp. 2972–3047, 2012.

[43] R. Bulla, T. a. Costi, and T. Pruschke, "Numerical renormalization group method for quantum impurity systems," *Reviews of Modern Physics*, vol. 80, no. 2, p. 395, 2008.

[44] Y. Xu, S. Uddin, J. Wang, J. Wu, and J.-F. Liu, "Penetration depth and nonlocal manipulation of quantum spin hall edge states in chiral honeycomb nanoribbons," *Scientific reports*, vol. 7, no. 1, p. 7578, 2017.

[45] W.-X. Wang, M. Zhou, X. Li, S.-Y. Li, X. Wu, W. Duan, and L. He, "Energy gaps of atomically precise armchair graphene sidewall nanoribbons," *Physical Review B*, vol. 93, no. 24, p. 241403, 2016.

[46] C.-H. Chung, D.-H. Lee, and S.-P. Chao, "Kane-mele hubbard model on a zigzag ribbon: Stability of the topological edge states and quantum phase transitions," *Physical Review B*, vol. 90, no. 3, p. 035116, 2014.

[47] A. Allerdt, A. E. Feiguin, and G. B. Martins, "Spatial structure of correlations around a quantum impurity at the edge of a two-dimensional topological insulator," *Physical Review B*, vol. 96, no. 3, p. 035109, 2017.

[48] A. Furusaki and N. Nagaosa, "Kondo effect in a tomonaga-luttinger liquid," *Physical review letters*, vol. 72, no. 6, p. 892, 1994.

[49] Y. Tanaka, A. Furusaki, and K. Matveev, "Conductance of a helical edge liquid coupled to a magnetic impurity," *Physical review letters*, vol. 106, no. 23, p. 236402, 2011.

[50] J. Maciejko, C. Liu, Y. Oreg, X.-L. Qi, C. Wu, and S.-C. Zhang, "Kondo effect in the helical edge liquid of the quantum spin hall state," *Physical review letters*, vol. 102, no. 25, p. 256803, 2009.

[51] V. Emery and S. Kivelson, "Mapping of the two-channel kondo problem to a resonant-level model," *Phys. Rev. B*, vol. 46, p. 10812, 1992.

Erklärung:

Hiermit erkläre ich, die vorliegende Arbeit selbständig verfasst zu haben und keine anderen als die in der Arbeit angegebenen Quellen und Hilfsmittel benutzt zu haben.

München, den 18.02.2019

Unterschrift: